

# Astrocytes Integrate Behavioral State and Vascular Signals during Functional Hyperemia

## Highlights

- Astrocyte  $\text{Ca}^{2+}$  follows functional hyperemia onset
- Astrocyte  $\text{Ca}^{2+}$  transients depend on the animal's behavioral state
- Astrocytes sense synaptic glutamate and vascular nitric oxide
- Direct arteriole activation facilitates astrocyte endfoot  $\text{Ca}^{2+}$

## Authors

Cam Ha T. Tran, Govind Peringod,  
Grant R. Gordon

## Correspondence

gordong@ucalgary.ca

## In Brief

Astrocytes influence brain processes via changes in free  $\text{Ca}^{2+}$ . What governs astrocyte  $\text{Ca}^{2+}$  transients in behaving animals is poorly understood. Tran et al. find that astrocytes are integrators of synaptic and vascular activity, which is influenced by animal locomotion.



# Astrocytes Integrate Behavioral State and Vascular Signals during Functional Hyperemia

Cam Ha T. Tran,<sup>1</sup> Govind Peringod,<sup>1</sup> and Grant R. Gordon<sup>1,2,\*</sup>

<sup>1</sup>Hotchkiss Brain Institute, Department of Physiology and Pharmacology, Cumming School of Medicine, University of Calgary, Calgary, AB T2N 4N1, Canada

<sup>2</sup>Lead Contact

\*Correspondence: [gordong@ucalgary.ca](mailto:gordong@ucalgary.ca)

<https://doi.org/10.1016/j.neuron.2018.09.045>

## SUMMARY

Dynamic changes in astrocyte free  $\text{Ca}^{2+}$  regulate synaptic signaling and local blood flow. Although astrocytes are poised to integrate signals from synapses and the vasculature to perform their functional roles, it remains unclear what dictates astrocyte responses during neurovascular coupling under realistic conditions. We examined peri-arteriole and peri-capillary astrocytes in the barrel cortex of active mice in response to sensory stimulation or volitional behaviors. We observed an AMPA and NMDA receptor-dependent elevation in astrocyte endfoot  $\text{Ca}^{2+}$  that followed functional hyperemia onset. This delayed astrocyte  $\text{Ca}^{2+}$  signal was dependent on the animal's action at the time of measurement as well as a neurovascular pathway that linked to endothelial-derived nitric oxide. A similar elevation in endfoot  $\text{Ca}^{2+}$  was evoked using vascular chemogenetics or optogenetics, and opto-stimulated dilation recruited the same nitric oxide pathway as functional hyperemia. These data show that behavioral state and microvasculature influence astrocyte  $\text{Ca}^{2+}$  in active mice.

## INTRODUCTION

Astrocytes are key players in the regulation of synapse strength and microcirculatory blood flow via changes in free intracellular  $\text{Ca}^{2+}$  at their peri-synaptic compartments and peri-vascular endfeet. Despite astrocytes' privileged position to integrate distinct inputs arising from both neurons and the microcirculation, our understanding of the factors governing astrocyte activation is limited in active animals during events that increase brain blood flow. In fact, coordinating brain activity with the delivery of blood must rely on local synapses, neuromodulatory networks, and vascular signals that operate dynamically across behavioral states, but how astrocyte activity fits into this complex control system is unclear. Examining  $\text{Ca}^{2+}$  signals in separate astrocyte compartments along with vasculature dynamics in behaving mice will provide insights into how these glial cells participate in brain energetics and plasticity.

Many studies have examined astrocyte  $\text{Ca}^{2+}$  signals in response to an experimental increase in neuronal activity. Evidence primarily from acute brain slices demonstrated that a change in astrocyte free  $\text{Ca}^{2+}$  was sufficient to actuate arteriole diameter (Girouard et al., 2010; Gordon et al., 2008; Mulligan and MacVicar, 2004; Rosenegger et al., 2015; Straub et al., 2006; Takano et al., 2006) and change synaptic efficacy (Fiocco and McCarthy, 2004; Gordon et al., 2009; Kang et al., 1998; Parpura and Haydon, 2000). Although *in vivo* work constitutes a significant technical advance, the majority of studies are limited in four primary aspects: (1) a preponderance of astrocyte soma or bulk astrocyte  $\text{Ca}^{2+}$  measurements with a lack of examination of the arbor or endfoot (Ding et al., 2013; Paukert et al., 2014; Schulz et al., 2012; Schummers et al., 2008; Takano et al., 2006); (2) use of electrical stimulation rather than a natural stimulus (Lind et al., 2013; Nizar et al., 2013; Schulz et al., 2012); (3) uncertainty regarding the origin of the  $\text{Ca}^{2+}$  signal from the use of bulk-loaded dyes (Lind et al., 2013; Schummers et al., 2008; Takano et al., 2007; Winship et al., 2007); and (4) use of anesthesia (Lind et al., 2013; Nizar et al., 2013; Otsu et al., 2015; Schulz et al., 2012; Schummers et al., 2008; Takano et al., 2007; Winship et al., 2007) or sedation (Bonder and McCarthy, 2014), which may misrepresent relationships between neural activity, astrocyte  $\text{Ca}^{2+}$  changes, and hemodynamics (Masamoto et al., 2009; Thrane et al., 2012; Tran and Gordon, 2015a).

Examining astrocytes in fully awake and active animals is critical because signaling pathways involving both the brain and the microcirculation can crosstalk in a realistic manner. Integration of local glutamatergic signaling with global noradrenergic (Ding et al., 2013; Paukert et al., 2014) or cholinergic (Chen et al., 2012; Takata et al., 2011) projections have been shown to enhance astrocyte  $\text{Ca}^{2+}$  signals. Additionally, work conducted in slices or under anesthesia *in vivo* suggests that astrocyte endfeet may sense changes in arteriole diameter (Kim et al., 2015; Kozlov et al., 2006). This further highlights the need to examine astrocytes in active preparations where microvascular diameter as well as local and long-range neuronal signaling are constantly changing. Recent reports regarding awake mice show novel  $\text{Ca}^{2+}$  dynamics in astrocytes (Agarwal et al., 2017; Bindocci et al., 2017; Paukert et al., 2014; Srinivasan et al., 2015; Stobart et al., 2018) but with no relationships to hemodynamics and with little new information provided regarding the factors that contribute to glutamate-evoked signals. Here we performed *in vivo* two-photon imaging on active mice to examine the  $\text{Ca}^{2+}$  activity patterns of cortical astrocytes during functional hyperemia.



## RESULTS

### Whisker Stimulation Induced Fast Functional Hyperemia followed by Delayed Astrocyte Ca<sup>2+</sup> Elevation

To investigate astrocyte activation under realistic conditions, we used our awake *in vivo* two-photon imaging model (Tran and Gordon, 2015b) adapted from previous technical advances (Dombeck et al., 2007; Shih et al., 2012) to image astrocyte free Ca<sup>2+</sup> and vasomotor responses to contralateral whisker stimulation (5-s air puff). Trained, head-restrained mice were free to ambulate on a passive air-supported spherical treadmill (Figure 1) and were video-monitored during fluorescence imaging to capture various behaviors, such as natural whisking and running, as well as to verify whisker deflection with an air puff (Figure 1A). We first employed *Slc1a3-Cre/ERT* x RCL-GCaMP3 mice to achieve a genetically encoded Ca<sup>2+</sup> indicator in astrocytes. This permitted the separate assessment of Ca<sup>2+</sup> dynamics in the soma, arbor, and endfoot of individual astrocytes surrounding penetrating arterioles in the barrel cortex (layers 1–3). The vasculature was visualized by labeling the blood plasma with Rhod B-dextran (Figures 1B and 1C). In response to whisker stimulation, functional hyperemia was consistently observed by the presence of fast arteriole dilation (onset = 0.8 s;  $\Delta d/d = 11.7\% \pm 1.1\%$ ,  $n = 155$  trials), which was followed by a delayed and widespread astrocyte Ca<sup>2+</sup> transient in the arbor (onset = 3.3 s;  $\Delta F/F = 13.5\% \pm 2.5\%$ ,  $n = 151$  trials), soma (onset = 3.3 s;  $\Delta F/F = 47.9\% \pm 10.5\%$ ,  $n = 64$  trials), and endfoot (onset = 3.9 s;  $\Delta F/F = 46.8\% \pm 8.5\%$ ,  $n = 147$  trials) (31 mice; Figures 1D and 1E; Video S1). These onset times were extrapolated from the averaged data (STAR Methods); thus, we also performed a trial-based analysis (STAR Methods) from a random selection of 90 trials (all onset time calculations were trial-based from here onward). This showed relatively slow Ca<sup>2+</sup> onsets for the soma ( $3.6 \pm 0.4$  s), arbor ( $3.9 \pm 0.3$  s), and endfoot ( $4.6 \pm 0.4$  s), all of which were significantly slower than the  $2.2 \pm 0.2$  s onset for arteriole dilation ( $p < 0.05$ ). This temporal profile of astrocyte Ca<sup>2+</sup> is in agreement with work in anesthetized mice (Nizar et al., 2013). However, in contrast to the low incidence of events described previously (~10%), our data showed that 65% of the trials exhibited a rise in endfoot Ca<sup>2+</sup> in active mice. Furthermore, 15% of these 90 trials showed arteriole dilation without a surge in Ca<sup>2+</sup>, 7% with an endfoot Ca<sup>2+</sup> rise without dilation, and 13% of trials without any response (Figure 1M). Summary astrocyte Ca<sup>2+</sup> data (Figure 1E) included all experimental trials and did not exclude failures; thus, the responses were relatively reliable.

We tested a shorter whisker stimulation duration and found that a 2-s air puff produced a similar arteriole dilatory response but with a less frequent endfoot Ca<sup>2+</sup> signal (56% versus 65%) with a smaller magnitude ( $28.3\% \pm 10.5\%$  versus  $74.4\% \pm 16.7\%$ ,  $n = 12$  trials, 7 mice,  $p = 0.03$ ; Figures 1G and 1H) compared with a 5-s air puff, suggesting that the length of stimulation facilitates astrocyte engagement. We next delivered a 5-s air puff to the vibrissae that were ipsilateral to the imaging window to drive transcallosal functional hyperemia. This triggered significantly smaller arteriole dilation ( $\Delta d/d = 12.2\% \pm 5.4\%$  versus  $28.4\% \pm 2.2\%$ ) with little astrocyte Ca<sup>2+</sup> signal ( $\Delta F/F = 8.6\% \pm 2.9\%$  versus  $145.0\% \pm 18.2\%$ ,  $n = 13$  trials, 5 mice).

Notably, because ipsilateral vibrissa stimulation failed to cause widespread astrocyte activation, this suggested that animal startle was minimal. Finally, we performed a control experiment where we puffed air away from the contralateral whiskers, not to deflect the vibrissae but to preserve the puffing sound. This had no effect on diameter ( $\Delta d/d = 7.65\% \pm 4.48\%$ ) or astrocyte Ca<sup>2+</sup> ( $\Delta F/F = 0.73\% \pm 2.90\%$ ,  $p > 0.05$ ,  $n = 8$  trials, 3 mice; Figures 1I and 1J), and suggested there was little auditory influence on our measurements. These experiments indicated that the arteriole dilation and Ca<sup>2+</sup> signals observed from whisker stimulation were due to whisker-related processing in the barrel.

Although GCaMP3 allows for unambiguous detection of Ca<sup>2+</sup> events from astrocyte compartments, the number of astrocytes exhibiting fluorescence and the signal-to-noise ratio of each cell achieved via knockin Cre-Lox crosses is inferior to a bulk-loaded synthetic Ca<sup>2+</sup> indicator. We repeated the above experiment using the relatively high-affinity probe Rhod-2 AM, which shows preferential loading into astrocytes (Takano et al., 2006). This strategy was used with blood plasma labeled with fluorescein isothiocyanate (FITC)-dextran (Figures 1K and 1L). An equivalent result was achieved as whisker stimulation elicited fast functional hyperemia (onset =  $2.1 \pm 0.3$  s,  $\Delta d/d = 20.6\% \pm 2.1\%$ ) that preceded the onset of a Rhod-2 astrocyte Ca<sup>2+</sup> signal in the arbor (onset =  $4.1 \pm 0.5$  s,  $\Delta F/F = 4.6\% \pm 2.0\%$ ), soma (onset =  $5.2 \pm 0.4$  s,  $\Delta F/F = 34.6\% \pm 11.1\%$ ,  $n = 41$  trials), and endfoot (onset =  $6.3 \pm 0.5$  s,  $\Delta F/F = 28.4\% \pm 6.1\%$ ) ( $n = 61$  trials, 18 mice; Figure 1M; Video S2).

We next compared these responses to astrocytes expressing GCaMP6s using *Aldh1l1-Cre/ERT2* x RCL-GCaMP6s (Ai96) mice. This was to improve both the magnitude of the  $\Delta F/F$  and the recombination efficacy (Srinivasan et al., 2016). Indeed, the magnitudes of the arbor and endfoot Ca<sup>2+</sup> signals were larger to 5-s whisker stimulation (GCaMP3 endfoot Ca<sup>2+</sup>  $\Delta F/F = 64.9\% \pm 12.5\%$ ,  $n = 69$  trials; 31 mice versus GCaMP6s endfoot Ca<sup>2+</sup>  $\Delta F/F = 169.6\% \pm 44.5\%$ ,  $n = 17$  trials; 5 mice,  $p = 0.001$ ; Figures 2A and 2B); however, the temporal profiles of arteriole dilation and astrocyte Ca<sup>2+</sup> were similar to our other approaches (GCaMP6s dilation onset:  $2.7 \pm 0.3$  s versus GCaMP3 dilation onset:  $2.2 \pm 0.2$  s;  $p = 0.1$ ; GCaMP6s endfoot Ca<sup>2+</sup> onset:  $6.0 \pm 0.8$  s versus GCaMP3 endfoot Ca<sup>2+</sup> onset:  $4.6 \pm 0.4$  s;  $p = 0.1$ ).

Previous work indicated that sensory stimulation initiates electrical conduction in capillaries (Longden et al., 2017) and triggers low-branch-order capillaries to dilate (Biesecker et al., 2016; Hall et al., 2014) before inducing penetrating arteriole dilation. Thus, we tested whether astrocyte endfoot Ca<sup>2+</sup> signals displayed different kinetics next to capillaries compared with those around arterioles in the superficial layers of the barrel cortex. In response to 5-s whisker stimulation, we measured an increase in RBC flux in capillaries (baseline:  $6.0 \pm 0.5$  RBCs/frame versus whisker stimulation:  $7.0 \pm 0.6$  RBCs/frame,  $n = 41$  trials, 11 mice,  $p < 0.001$ ) and a large Ca<sup>2+</sup> signal in peri-capillary endfeet, arbors, and somata (Figures 2C–2E). The capillary endfoot Ca<sup>2+</sup> showed a significantly faster onset time compared with peri-arteriole endfeet (GCaMP3 capillary endfoot Ca<sup>2+</sup> onset:  $3.0 \pm 0.5$  s,  $n = 29$  trials, 11 mice versus GCaMP3 arteriole endfoot Ca<sup>2+</sup> onset:  $4.6 \pm 0.4$  s,  $n = 90$  trials, 31 mice,  $p = 0.01$ ; Figure 2F). In these experiments, most of the capillaries were greater than three branch orders from the zero-order penetrator, and we

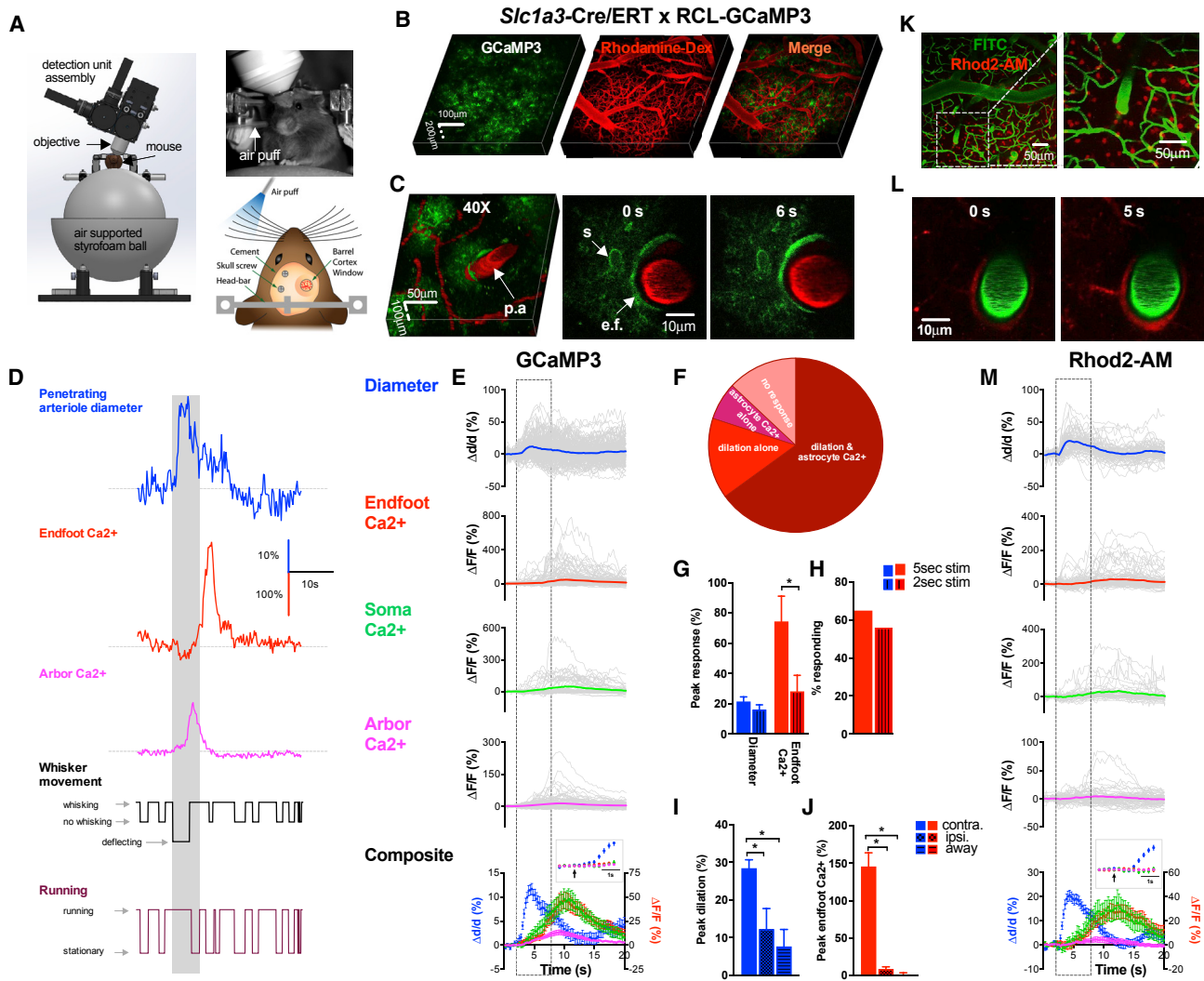


**Figure 1. Whisker Stimulation Generated Fast Penetrating Arteriolar Dilation That Was Followed by a Delayed Astrocyte  $\text{Ca}^{2+}$  Transient**

(A) Schematics and image of the awake mouse experimental setup.

(B) 3D reconstruction of the barrel cortex from a *Slc1a3-Cre/ERT* RCL-GCaMP3 mouse. Shown are astrocytes (green) and vascular Rhod B-dextran (red).

(C) Close-up z stack of a penetrating arteriole (p.a.) (red) and astrocytes (green) (left), penetrating arteriole wrapped by an endfoot (e.f.) with nearby soma (s) before whisker stimulation (0 s, center), and vasodilation with astrocyte  $\text{Ca}^{2+}$  elevation (6 s, right).

(D) Representative data from a *Slc1a3-Cre/ERT* RCL-GCaMP3 mouse showing arteriole diameter, endfoot  $\text{Ca}^{2+}$ , and arbor  $\text{Ca}^{2+}$  in response to whisker stimulation, along with categorized whisker movement and treadmill running. Shaded area indicates whisker stimulation.

(E) Time courses of arteriolar diameter and  $\text{Ca}^{2+}$  measurements in astrocyte GCaMP3 mice from all experiments (individual trial traces are shown in gray, and average traces are shown in color). Summary traces are shown at the bottom. Inset: onset of signals for temporal comparison. Vertical dotted area indicates whisker stimulation.

(F) Percentage of trials that generated different combinations of responses to whisker stimulation.

(G) Summary data of peak dilation and endfoot  $\text{Ca}^{2+}$  in response to 5-s and 2-s whisker stimulation.

(H) The percentage of trials generating endfoot  $\text{Ca}^{2+}$  signals in response to 5-s and 2-s whisker stimulation.

(I and J) Summary data in response to 5-s whisker stimulation delivered contralaterally, ipsilaterally, and away for vasodilation (I) and endfoot  $\text{Ca}^{2+}$  (J).

(K) Barrel cortex from a C57BL/6J mouse with FITC-dextran vasculature and astrocytes loaded with Rhod-2 AM.

(L) Penetrating arteriole and endfoot response immediately prior to (0 s) and after (5 s) whisker stimulation.

(M) Same as (E) but for Rhod-2 AM-loaded astrocytes in C57BL/6J mice.

\* $p < 0.05$ . Data are mean  $\pm$  SEM.

did not detect an increase in capillary diameter to whisker stimulation at this level in the network ( $-0.5\% \pm 0.7\%$ ,  $n = 41$  trials, 11 mice,  $p = 0.5$ ), consistent with previous results (Cai et al.,

2018). These faster capillary endfoot  $\text{Ca}^{2+}$  signals are consistent with the idea that capillaries sense cortical signals before arterioles. However, because peri-capillary astrocyte  $\text{Ca}^{2+}$  still lagged

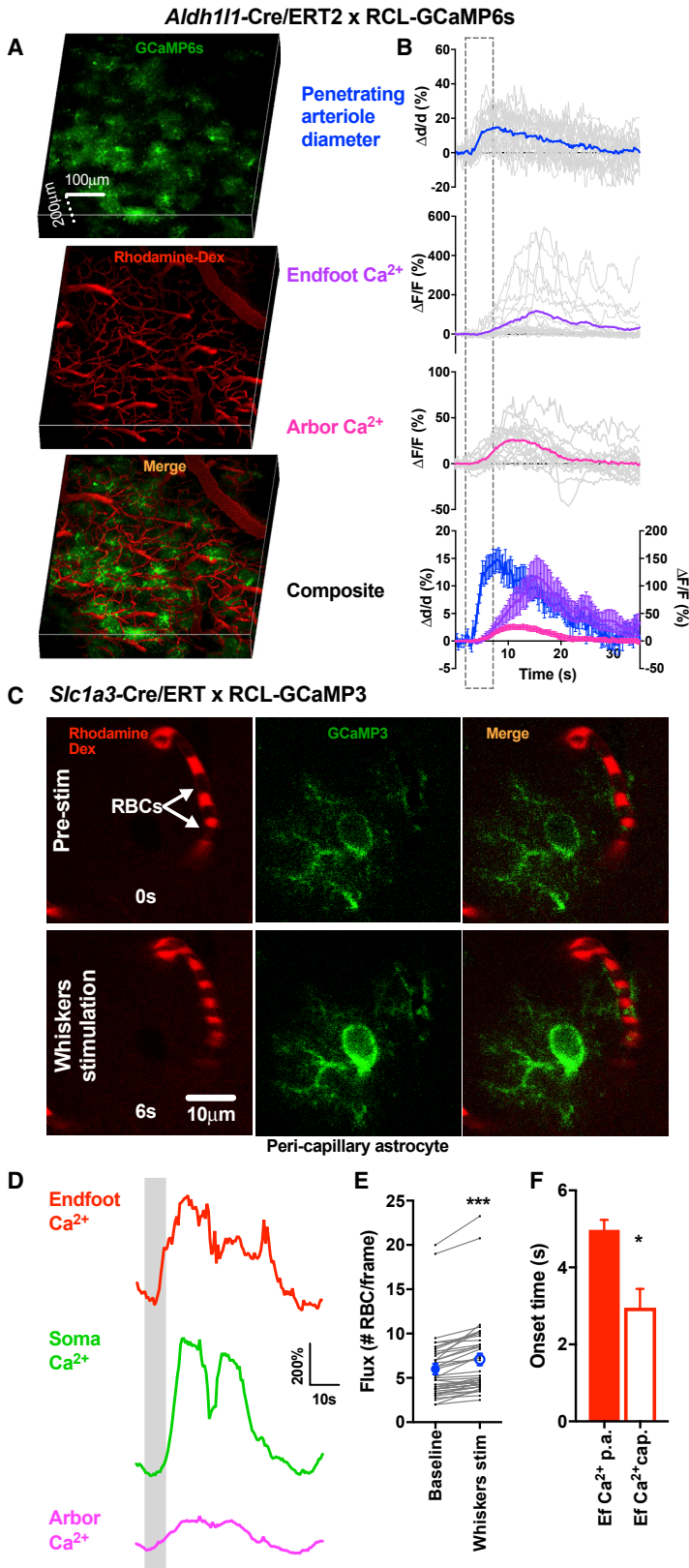


**Figure 2. Whisker Stimulation Generated Delayed Astrocytic Endfoot  $Ca^{2+}$  in *Aldh111-Cre/ERT2* GCaMP6s Mice at Arterioles and at the Capillary Level**

(A) z stack of the barrel cortex from an *Aldh111-Cre/ERT2* RCL-GCaMP6s mouse. Shown are astrocytes (green) and vascular RhodB-dextran (red).

(B) Time courses of arteriolar diameter and astrocyte  $Ca^{2+}$  from all experiments (individual trial traces are shown in gray, and average traces are shown in color) ( $n = 21$  trials, 5 animals). Summary traces are shown at the bottom. Dotted area indicates whisker stimulation.

(C) Capillary and astrocyte from *Slc1a3-Cre/ERT* RCL-GCaMP3 mice prior to (0 s) and in response (6 s) to whisker stimulation.

(D) Representative astrocyte  $Ca^{2+}$  traces in response to whisker stimulation. Shaded area indicates whisker stimulation.

(E) Summary data of red blood cell flux at baseline and in response to whisker stimulation ( $n = 14$ ,  $***p < 0.001$ , paired t test).

(F) Summary of onset time of astrocytic endfoot  $Ca^{2+}$  from enveloping penetrating arterioles or capillaries (cap) ( $*p = 0.02$ , unpaired t test). Data are mean  $\pm$  SEM.

functional hyperemia onset (arteriole initiation = 0.8 s), this suggests that this particular delayed  $\text{Ca}^{2+}$  signal is not an initiator of the blood flow increase. However, we cannot exclude a role for ultrafast (Lind et al., 2013) or small  $\text{Ca}^{2+}$  transients in astrocytes (Bindocci et al., 2017; Stobart et al., 2018) below our sampling/detection threshold, nor can we rule out  $\text{Ca}^{2+}$  signals in the deeper layers of the cortex, where functional hyperemia could initiate (Uhlirova et al., 2016). Thus, we chose to explore potential factors governing this robust but delayed  $\text{Ca}^{2+}$  signal during sensory stimulation.

### Animal Behavioral State Dictates the Magnitude of Delayed Astrocyte $\text{Ca}^{2+}$ Signals

Behavioral states such as arousal, attention, and locomotion have been proposed to prime astrocytes in response to local neuronal activity in the neocortex (Paukert et al., 2014; Takata et al., 2011). These findings implicate an interaction between neuromodulatory networks and local glutamatergic signaling in controlling astrocyte  $\text{Ca}^{2+}$  activity, with analogous processes occurring in organisms as simple as flies (Ma et al., 2016). However, whether this relationship is also observed between astrocyte endfeet and the microvasculature during sensation-evoked blood flow increases in awake mice remains unexplored. We analyzed our large dataset to test whether the animal's behavior would predict some of the variability we observed in astrocyte responses. Examining a subset of the data (41 trials encompassing 25 arterioles and astrocytes from 21 mice), where we could clearly categorize a given animal's action, revealed three primary behavioral states that were associated with whisker stimulation: quiet-to-running, in which animals were resting prior to but started running immediately after the stimulation onset (13 trials); continuous running, identifying animals that were running prior to and remained running during the stimulation period (21 trials); and continuous quiet, indicating animals that remained quiet before, during, and after whisker stimulation (7 trials) (Figure 3A). Histogram and scatterplot analyses of the response onset and peak of all 41 trials demonstrated tightly clustered arteriole dilation data, whereas endfoot  $\text{Ca}^{2+}$  responses were variable between the three different behavioral states (Figures 3B–3F). Notably, the behavioral state did not affect the onset time of arteriole dilation (quiet-to-running,  $1.7 \pm 0.4$  s; continuous running,  $2.3 \pm 0.3$  s; continuous quiet,  $1.9 \pm 0.3$  s;  $p > 0.05$ ; Figure 3G) or the onset of endfoot  $\text{Ca}^{2+}$  rise (quiet-to-running,  $3.9 \pm 0.6$  s; continuous running,  $5.7 \pm 0.7$  s; continuous quiet,  $3.9 \pm 0.8$  s;  $p > 0.05$ ; Figure 3H). Although the peak amplitude of dilation was also not influenced by different behavioral states (quiet-to-running,  $27.1\% \pm 3.2\%$ ; continuous running,  $26.2\% \pm 2.6\%$ ; continuous quiet,  $39.5\% \pm 8.7\%$ ;  $p > 0.05$ ; Figure 3I), we observed a significant difference between the peak amplitude of endfoot  $\text{Ca}^{2+}$  transients. In particular, when whisker stimulation triggered running, a significantly stronger endfoot  $\text{Ca}^{2+}$  signal was observed (quiet-to-running,  $\Delta F/F = 241.9\% \pm 30.4\%$ ) compared with when the animal was constantly running ( $\Delta F/F = 133.5\% \pm 20.8\%$ ,  $p = 0.006$ ). Notably, continuous quiet mice, suggestive of an un-engaged behavior, generated the smallest  $\text{Ca}^{2+}$  transients ( $\Delta F/F = 17.5\% \pm 2.9\%$ ) that were significantly different from the other two conditions ( $p = 0.02$ ,  $p < 0.001$ ; Figure 3J). These data suggest that the magnitude

of the late astrocyte endfoot  $\text{Ca}^{2+}$  signal during neurovascular coupling is potentiated by movement.

### Volitional Behaviors Cause Functional Hyperemia and Delayed Endfoot $\text{Ca}^{2+}$ Signals

Running is tightly associated with natural whisking in mice and rats (Sofroniew and Svoboda, 2015), a relationship we also observed in our data (Figure 1D). The barrel cortex is reciprocally connected with whisker motor regions (Deschênes et al., 2012), suggesting that the act of whisking may drive neural activity and blood flow changes in the barrel. Therefore, we aimed to examine arteriole diameter changes and endfoot  $\text{Ca}^{2+}$  activity in response to volitional running where the animal naturally whisked (e.g., a quiet-to-running behavior without whisker stimulation). We analyzed activities associated with volitional movement that lasted more than 2 s and that were separated from any previous volitional movement (Figure 4A; Video S3) ( $n = 23$  trials, 10 mice). This may be particularly important because natural whisking and experimental whisker deflection have been demonstrated to rely on distinct afferent inputs and signal processing mechanisms within the somatosensory cortex (Arabzadeh et al., 2005; Krupa et al., 2004). Interestingly, volitional running and natural whisking induced a robust functional hyperemia that was again followed by a delayed astrocyte  $\text{Ca}^{2+}$  transient (Figures 4B–4F). Although natural whisking and the deflection of whiskers via air puff generated arteriole dilation with a similar onset (natural:  $1.5 \pm 0.2$  s versus stimulation:  $1.7 \pm 0.4$  s,  $p = 0.7$ ; Figure 4G), the peak dilation was significantly larger for the volitional behavior (natural:  $43.4\% \pm 5.7\%$  versus stimulation:  $27.1\% \pm 3.2\%$  versus  $p = 0.02$ ; Figure 4H). Additionally, the onset time of the volitional running-induced endfoot  $\text{Ca}^{2+}$  increase was significantly more delayed than that of whisker deflection (natural:  $6.8 \pm 0.7$  s versus stimulation:  $3.9 \pm 0.6$  s,  $p = 0.008$ ; Figure 4I). Furthermore, when the animal chose to go from being quiet to running, the peak endfoot  $\text{Ca}^{2+}$  signal generated was significantly smaller than that observed when the animal went from quiet to running in response to whisker stimulation (natural:  $123.8\% \pm 30.1\%$  versus stimulation:  $241.9\% \pm 30.4\%$ ,  $p = 0.004$ ; Figure 4J). These data provide evidence that experimental whisker deflection and natural whisking result in different measurable outcomes regarding both arteriole diameter and astrocyte  $\text{Ca}^{2+}$  transients in the barrel cortex of the awake animal.

### Glutamatergic Signaling Is Necessary for the Sensation-Evoked Delayed Astrocyte $\text{Ca}^{2+}$ Rise

Afferent glutamatergic input from the thalamus to the neocortex is an important initiation signal for functional hyperemia in anesthetized animals (Norup Nielsen and Lauritzen, 2001) and can mediate synaptically evoked astrocyte  $\text{Ca}^{2+}$  transients in the barrel cortex and the olfactory bulb (Lind et al., 2013; Otsu et al., 2015). To test for a contribution from this pathway in awake mice, we topically administered the ionotropic, non-NMDA receptor antagonist DNQX (500  $\mu\text{M}$ ) to the surface of the neocortex. By employing a cranial window in which the cover glass was perforated with multiple  $\sim 175\text{-}\mu\text{m}$  diameter through-holes, we could maintain the same basic imaging configuration and stability as our previous control trials while

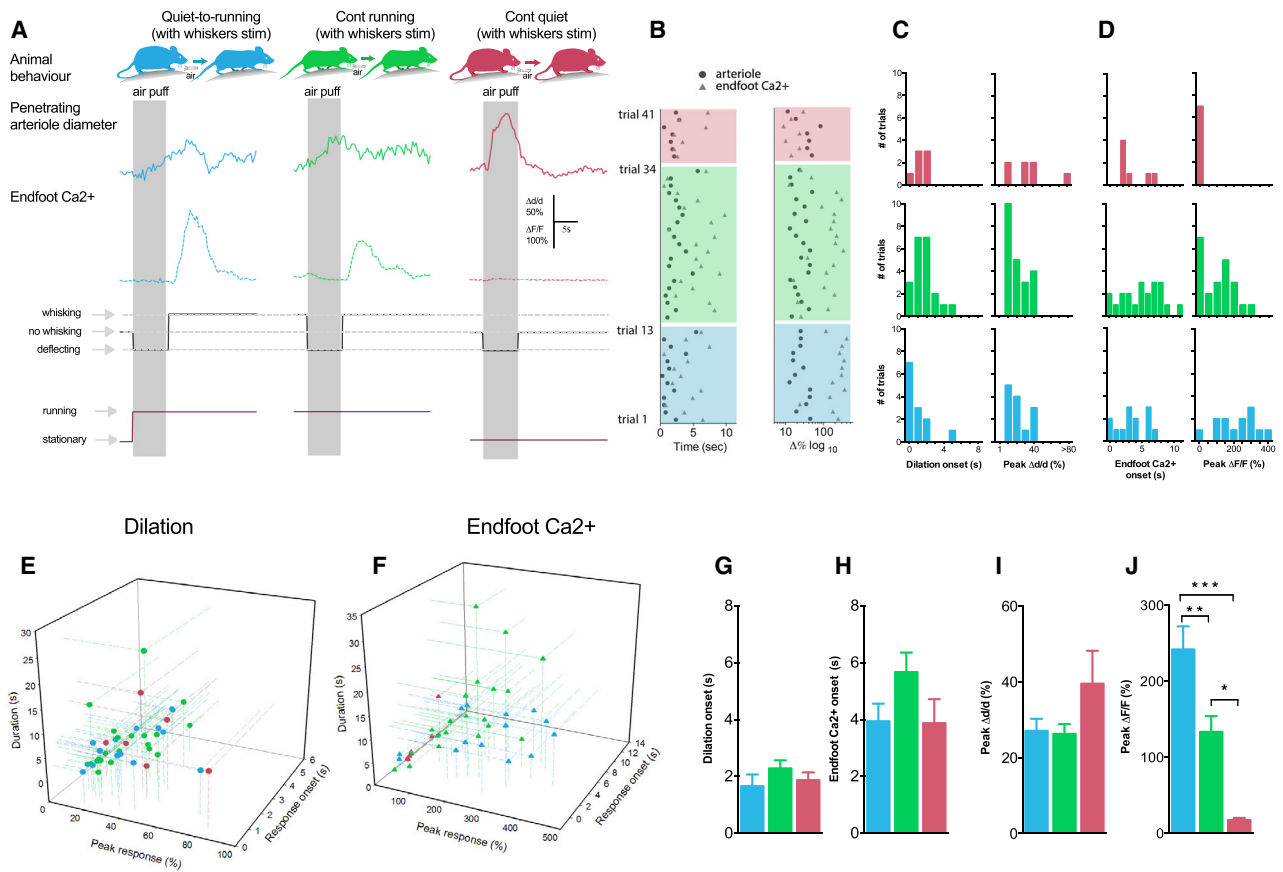


**Figure 3. Delayed Astrocyte Endfeet  $\text{Ca}^{2+}$  Transients Were Dependent on the Behavioral State**

(A) Representative traces of arteriole diameter and endfoot  $\text{Ca}^{2+}$  in response to whisker stimulation and the corresponding behavioral states. Left: quiet-to-running (cyan,  $n = 13$  trials). Center: continuous running (green,  $n = 21$  trials). Right: continuous quiet (burgundy,  $n = 7$  trials). “Deflecting” indicates whiskers deflected by an air puff. Shaded areas indicate whisker stimulation.

(B) Plots of response onset (left) and peak response (right) for each trial (horizontal pairs) categorized into different behavioral states.

(C) Distribution histograms of dilation onset and peak dilation for each behavioral state.

(D) Same as (C) but for endfoot  $\text{Ca}^{2+}$ .

(E) 3-axis scatterplot of dilation onset, peak, and duration, color-coded for behavior.

(F) Same as (E) but for endfoot  $\text{Ca}^{2+}$ .

(G and H) Summary data of dilation (G) and endfoot  $\text{Ca}^{2+}$  (H) transient onset for each behavioral state.

(I and J) Summary data of peak dilation (I) and peak endfoot  $\text{Ca}^{2+}$  elevation (J) for each behavioral state. \* $p < 0.05$ , \*\* $p < 0.01$ , \*\*\* $p < 0.001$ , one-way ANOVA. Data are mean  $\pm$  SEM.

being able to superfuse compounds (Figure 5A). Performing a paired comparison of control trials (superfused aCSF) to trials in the presence of DNQX, we found that DNQX only marginally reduced the evoked arteriole dilation ( $\Delta d/d = 31.6\% \pm 4.0\%$  versus  $27.6\% \pm 4.1\%$ ,  $p = 0.9$ ; Figures 5B and 5C) but robustly inhibited  $\text{Ca}^{2+}$  transients in the endfoot ( $\Delta F/F = 90.6\% \pm 17.3\%$  versus  $31.4\% \pm 15.6\%$ ,  $n = 21$  trials; 9 mice,  $p = 0.005$ ; Figures 5B and 5D). NMDA receptor activation is also a key pathway in functional hyperemia (Fergus and Lee, 1997) and in synaptically evoked astrocyte  $\text{Ca}^{2+}$  elevations (Dani and Smith, 1995; Mehina et al., 2017). Superfusing the competitive NMDA receptor (NMDAR) antagonist DL-APV (1 mM) had similar effects to DNQX, producing little attenuation of arteriole dilation ( $\Delta d/d = 24.6\% \pm 2.0\%$  versus  $20.3\% \pm 2.8\%$ ,  $p = 0.1$ ; Figure 5C) while significantly decreasing the elevation in end-

foot  $\text{Ca}^{2+}$  ( $\Delta F/F = 77.5\% \pm 12.9\%$  versus  $43.7\% \pm 11.2\%$ ,  $n = 27$  trials; 5 mice,  $p = 0.02$ ; Figure 5D). The fact that arteriole dilation was largely maintained by DNQX and APV was likely the result of insufficient concentration at a depth where functional hyperemia initiates (Tian et al., 2010). In line with this idea, we found that the same concentration of DNQX significantly attenuated naturally occurring functional hyperemia in the barrel cortex in response to a running/whisking event ( $\Delta d/d = 43.4\% \pm 5.6\%$  versus  $23.3\% \pm 4.0\%$ ,  $n = 10$  trials, 5 mice,  $p = 0.006$ ). Here, one would expect a stronger contribution of associative inputs in superficial layers (Muralidhar et al., 2013) where the DNQX concentration was highest. These data demonstrate an essential role for ionotropic, non-NMDA, and NMDA glutamate receptor activation in generating the late  $\text{Ca}^{2+}$  signal in astrocyte endfeet.

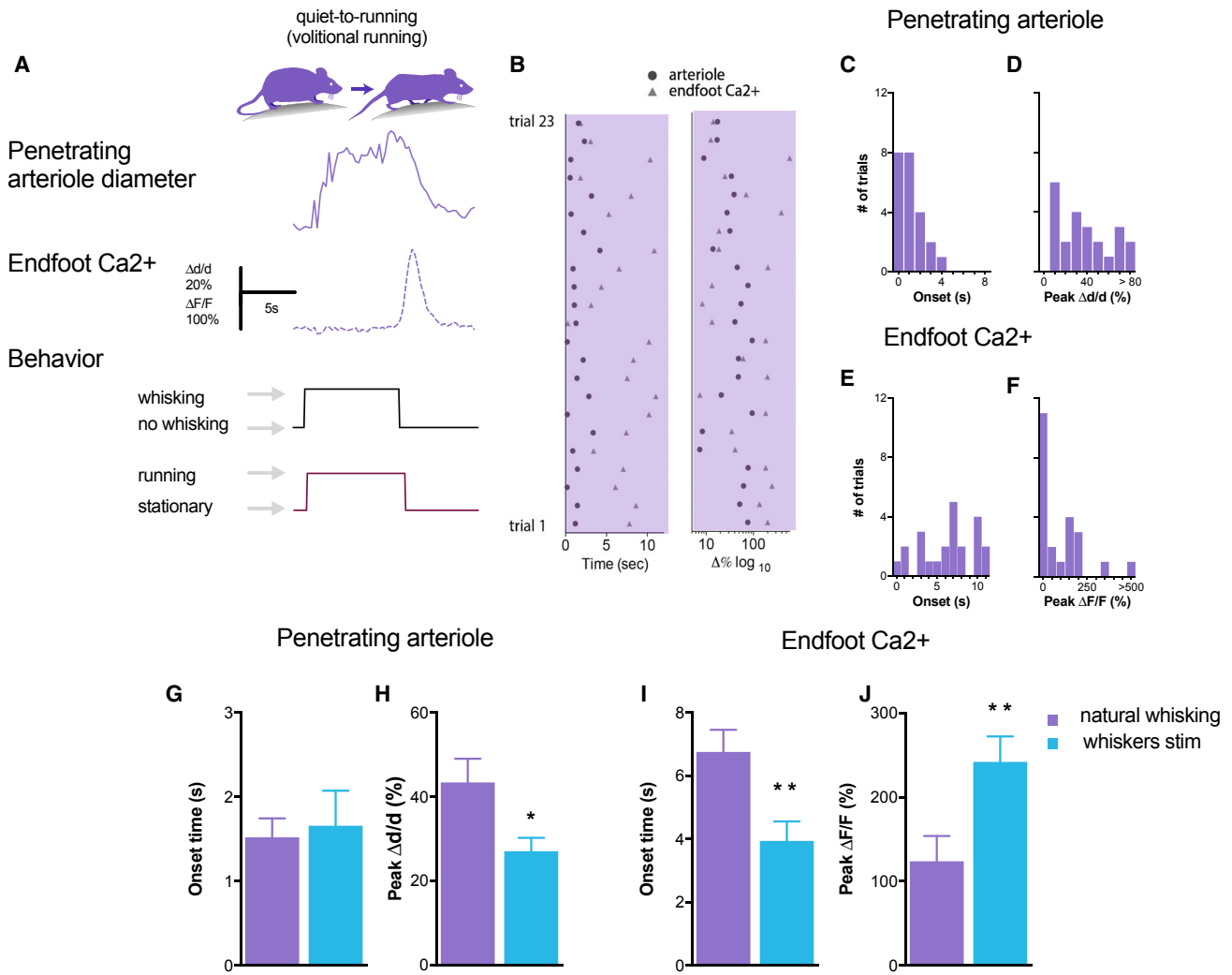


**Figure 4. Natural Running/Whisking Produced Arteriole Dilation with a Delayed Astrocyte  $\text{Ca}^{2+}$  Transient**

(A) Representative traces of diameter and endfoot  $\text{Ca}^{2+}$  acquired when the animal transitioned from quiet wakefulness to volitional running/whisking without experimental whisker stimulation.

(B) Plots of response onset (left) and peak response (right) for each trial. Arteriolar dilation and endfoot  $\text{Ca}^{2+}$  from a given trial are paired horizontally.

(C–F) Distribution histograms of response onset for vasodilation (C) and endfoot  $\text{Ca}^{2+}$  (E), and peak response for vasodilation (D) and endfoot  $\text{Ca}^{2+}$  (F) for natural running/whisking.

(G and H) Summary graphs of vasodilation onset (G) and peak dilation (H) for natural running/whisking (purple) compared with experimental whisker stimulation (cyan).

(I and J) Summary graphs of endfoot  $\text{Ca}^{2+}$  onset (I) and peak endfoot  $\text{Ca}^{2+}$  rise (J) during natural running/whisking compared with whisker stimulation.

\* $p < 0.05$  and \*\* $p < 0.01$ , unpaired t test. Data are mean  $\pm$  SEM.

### The Delayed Endfoot $\text{Ca}^{2+}$ Signal Is Modulated by Distinct Neurovascular Coupling Pathways

To better understand the relationship between functional hyperemia and the delayed astrocyte endfoot  $\text{Ca}^{2+}$  signal, we tested the effect of pharmacologically antagonizing cyclooxygenase-2 (COX-2) and nitric oxide synthases (NOSs), vasoactive enzymes that are downstream of AMPA and NMDA receptor activation. Because prostaglandins can elevate astrocyte  $\text{Ca}^{2+}$  (Bezzi et al., 1998), and nitric oxide (NO) can either directly elevate astrocyte  $\text{Ca}^{2+}$  (Bal-Price et al., 2002) or facilitate astrocyte  $\text{Ca}^{2+}$  elevations to glutamate (Pasti et al., 1995), we tested

whether these neural mediators increased astrocyte  $\text{Ca}^{2+}$ . Additionally, we pondered whether a general reduction in functional hyperemia would reduce the delayed astrocyte  $\text{Ca}^{2+}$  signal or whether a specific neurovascular coupling pathway was involved. First, we antagonized COX-2 with SC58125 (50  $\mu\text{M}$ ). Using perforated glass windows, the local superfusion of SC58125 into the barrel cortex resulted in decreased sensory evoked arteriole dilation as anticipated ( $\Delta\text{d}/\text{d} = 27.7\% \pm 4.3\%$  versus  $12.3\% \pm 2.9\%$ ,  $p = 0.02$ ; Figures 6A and 6B), but there was no effect on the evoked endfoot  $\text{Ca}^{2+}$  signal ( $\Delta\text{F}/\text{F} = 58.2\% \pm 22.4\%$  versus  $39.3\% \pm 16.4\%$ ,  $n = 15$  trials, 5 mice,

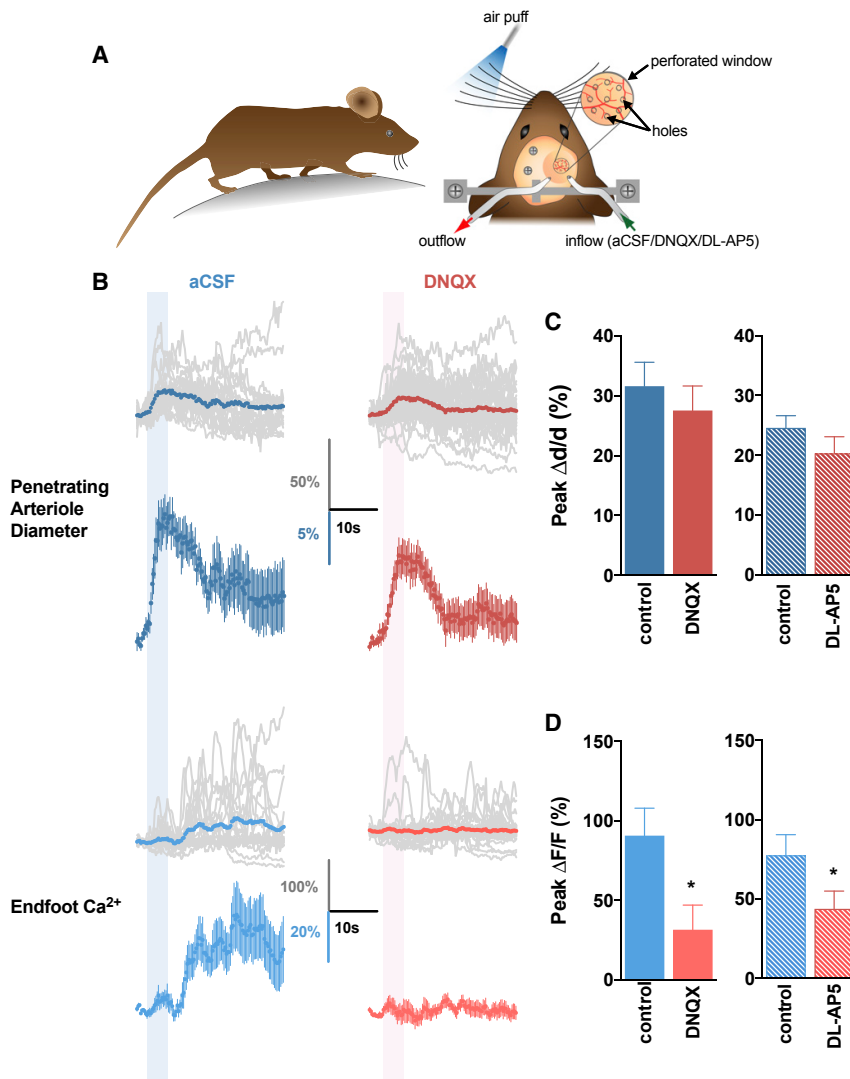


### Figure 5. Blockade of Ionotropic Glutamate Receptors Inhibited Delayed Astrocyte $\text{Ca}^{2+}$ Transients

(A) Cartoon depicting the experimental configuration for the superfusion of aCSF or aCSF + DNQX/DL-AP5 into the barrel cortex through a perforated glass cranial window.

(B) Time courses of diameter and endfoot  $\text{Ca}^{2+}$  in response to whisker stimulation in the absence (left) or presence (right) of DNQX. Shaded areas indicate whisker stimulation.

(C) Summary vasodilation data in DNQX (left) ( $n = 21$  trials, 10 animals) or DL-AP5 (right) ( $n = 27$  trials, 5 animals). Data are mean  $\pm$  SEM.

(D) Summary endfoot  $\text{Ca}^{2+}$  data in DNQX ( $*p < 0.05$ ) or DL-AP5 ( $*p = 0.02$ ). Paired  $t$  test. Data are mean  $\pm$  SEM.

(vasoconstriction) (normalized baseline diameter =  $82.7\% \pm 5.2\%$ ,  $n = 4$ ,  $p = 0.0003$ ), which is consistent with the ongoing production of NO from shear-stress activated eNOS (NOS3) in the vascular endothelium (Chatterjee et al., 2015). Furthermore, the partially constricted vessel in LNIO displayed increased peak arteriole dilation in response to whisker stimulation (control  $\Delta d/d = 26.9\% \pm 2.4\%$  versus LNIO  $\Delta d/d = 36.2\% \pm 3.2\%$ ,  $p = 0.01$ ). Interestingly, the evoked endfoot  $\text{Ca}^{2+}$  signal in LNIO was significantly reduced (control  $\Delta F/F = 79.3\% \pm 13.9\%$  versus LNIO  $\Delta F/F = 34.8\% \pm 8.1\%$ ,  $n = 36$  trials; 4 mice,  $p = 0.002$ ; Figures 6E and 6F). These data suggest that the late endfoot  $\text{Ca}^{2+}$  signal is modulated by distinct blood flow control pathways, likely involving an increase in vessel-derived NO from the

$p = 0.7$ ; Figures 6A and 6B). Additionally, there was no effect on baseline arteriole tone from SC58125 (normalized baseline diameter:  $83.5\% \pm 16.6\%$ ,  $n = 5$ ,  $p = 0.4$ ; Figure 6B). To target NOS, we first used LNPLA to block nNOS (NOS1), which has 150-fold selectivity over eNOS (NOS3) (Zhang et al., 1997). The local superfusion of LNPLA ( $300 \mu\text{M}$ ) decreased sensory evoked arteriole dilation (control  $\Delta d/d = 20.9\% \pm 2.0\%$  versus LNPLA  $\Delta d/d = 15.8 \pm 4.1$ ,  $p = 0.04$ ; Figures 6C and 6D) but was without significant effect on endfoot  $\text{Ca}^{2+}$  ( $\Delta F/F = 48.8\% \pm 11.6\%$  versus  $61.73\% \pm 12.4\%$ ,  $n = 35$  trials; 5 mice,  $p = 0.07$ ; Figures 6C and 6D). Consistent with a selective action on nNOS, we found no change to resting arteriole tone by the application of LNPLA into the barrel cortex (normalized baseline diameter:  $94.7\% \pm 3.8\%$ ,  $n = 5$ ,  $p > 0.9$ ; Figure 6D). Notably, these results were distinctly different from what we observed using the non-selective NOS inhibitor LNIO ( $300 \mu\text{M}$ ), which has been demonstrated in some experiments to have preferential action on eNOS over nNOS (Jiang et al., 2002). Superfusion of LNIO significantly increased basal arteriole tone

arteriole dilation, which is consistent with the delayed nature of the endfoot  $\text{Ca}^{2+}$  signal.

### Microvasculature Can Elevate Endfoot $\text{Ca}^{2+}$

Given that astrocyte endfoot  $\text{Ca}^{2+}$  follows the peak of arteriole dilation and that putative eNOS blockade reduced the late endfoot  $\text{Ca}^{2+}$  signal, we hypothesized that increased blood flow via increased arteriole diameter contributes to elevating endfoot  $\text{Ca}^{2+}$ . A similar concept involving astrocyte sensing of intraluminal pressure pulses (Kozlov et al., 2006) or vasoconstriction from the myogenic response (Kim et al., 2015) has been forwarded, with most evidence from acute brain slices. However, little is known about how vasculature may communicate to astrocytes in awake mice. To test our hypothesis, we selectively manipulated vascular responses using chemogenetics and monitored astrocyte  $\text{Ca}^{2+}$  dynamics (Figure 7A). Activation of endogenous Gq-coupled receptors in endothelium, such as muscarinic 5, is known to drive vasodilation in cerebral arterioles (Yamada et al., 2001). Therefore, we activated hm3Dq receptors

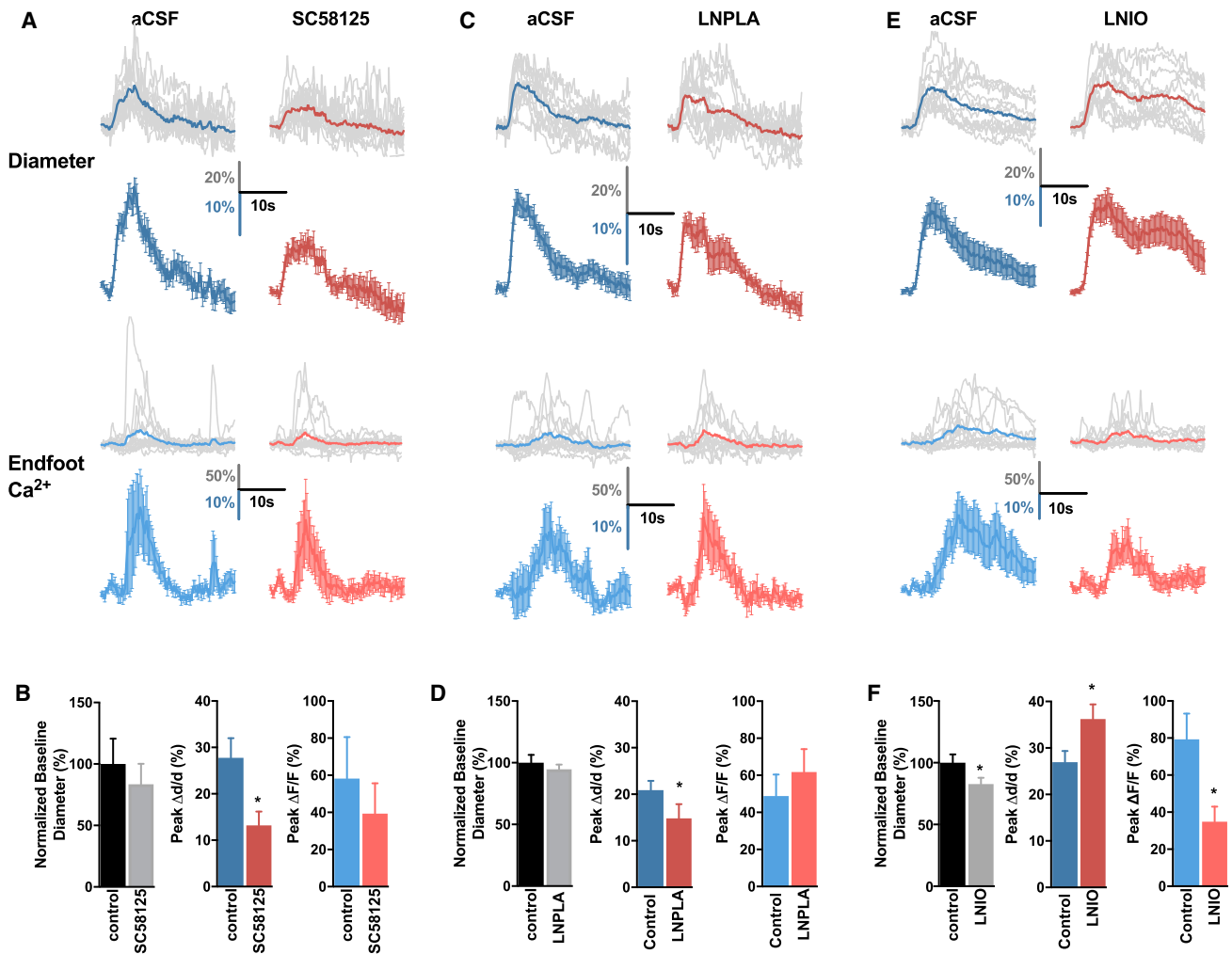


**Figure 6. Blockage of COX-2 or NOS Differential Affects Endfoot  $\text{Ca}^{2+}$  and Functional Hyperemia**

(A) Arteriole diameter (top) and endfoot  $\text{Ca}^{2+}$  (bottom) time course in response to whisker stimulation in the absence or presence of the COX-2 antagonist SC58125. Raw individual trial traces (gray) with average (color) are shown above. Summary traces with SEM are shown below.

(B) Summary of change in basal tone by SC58125 (left), evoked vasodilation (center), and evoked endfoot  $\text{Ca}^{2+}$  (right) in the presence or absence of SC58125 ( $n = 15$  trials, 5 animals) \* $p = 0.01$ , paired t test. Data are mean  $\pm$  SEM.

(C) Same as (A) but in the presence or absence of the nNOS blocker LNPLA.

(D) Same as (B) but for LNPLA ( $n = 34$  trials, 7 animals) \* $p = 0.04$ , paired t test. Data are mean  $\pm$  SEM.

(E) Same as (A) but in the presence or absence of the NOS blocker LNIO.

(F) Same as (B) but for LNIO ( $n = 36$  trials, 5 animals). Paired t test. Data are mean  $\pm$  SEM.

expressed in vascular endothelium using *Tek-Cre/ERT2* x *CAG-LSL-Gq-DREADD* mice. The mCitrine reporter for the Gq-DREADD showed selective vascular endothelial expression in the barrel cortex (Figure 7B). After verification of the mCitrine signal, mice were tail vein-injected with FITC dextran. Tissue was loaded with Rhod-2 AM to label astrocytes during window installation. Local superfusion of the hM3Dq ligand compound 21 (50  $\mu\text{M}$ ) generated large and sustained dilation of the penetrating arteriole ( $\Delta d/d = 30.1\% \pm 9.8\%$ ,  $p = 0.002$ ; Figures 7C–7E), which was followed by a delayed elevation in endfoot  $\text{Ca}^{2+}$  ( $\Delta F/F = 15.2\% \pm 7.3\%$ ,  $n = 10$  mice,  $p = 0.005$ ; Figures 7C–7E) (onset time,  $111 \pm 47$  s) (Video S4). This effect was not observed in animals negative for both knockin sequences

( $\Delta d/d = -1.52\% \pm 2.1\%$ ,  $\Delta F/F = -13.4\% \pm 3.6\%$ ,  $n = 5$  mice,  $p = 0.6$ ; Figure 7D). Gq receptor activation in endothelium couples to NO production (Palmer et al., 1987); thus, we tested the role of vascular NO in these effects. In the presence of LNIO, both arteriole dilation ( $\Delta d/d = 8.1\% \pm 7.0\%$ ,  $p = 0.02$ ) and the elevation in endfoot  $\text{Ca}^{2+}$  ( $\Delta F/F = -7.1\% \pm 5.3\%$ ,  $n = 10$  mice,  $p = 0.04$ ) were significantly reduced during compound 21 application (Figure 8E).

We then used optogenetics for an additional strategy to test for a direct or facilitating effect of the vasculature on astrocyte endfoot  $\text{Ca}^{2+}$  dynamics. We used *Tek-Cre* x *ArchT/EGFP* mice in which vascular endothelial cells expressed a light-sensitive proton pump (Figures 8A and 8B; Video S5). The rationale was

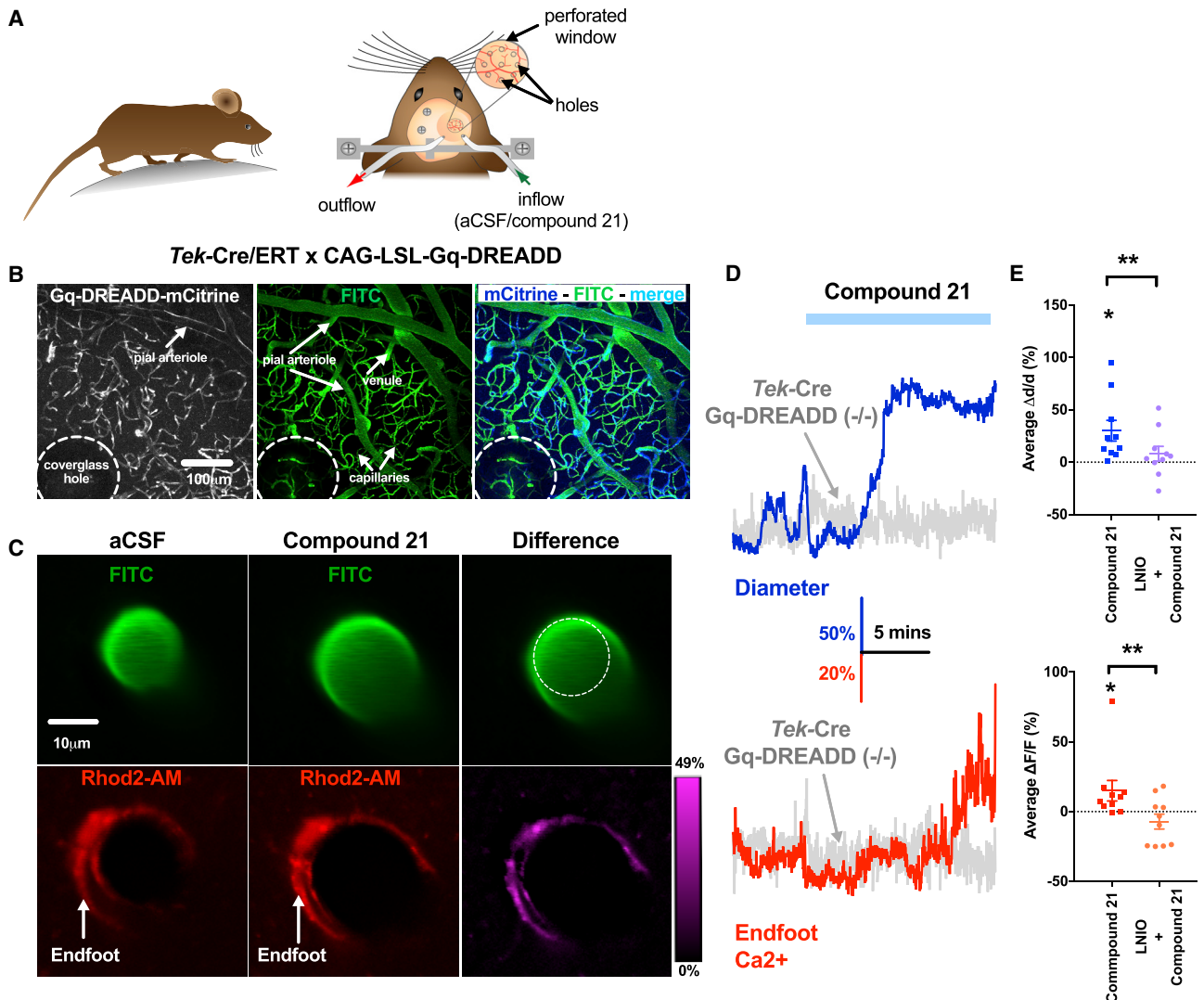


**Figure 7. Arteriole Dilation Triggered by Vascular Endothelium Gq-DREADD Evoked NO-Dependent Endfoot  $Ca^{2+}$  Elevation**

(A) Cartoons depicting the configuration for superfusion of compound 21 (50  $\mu$ M) in an awake mouse.

(B) Barrel cortex from a *Tek-Cre/ERT2 Gq-DREADD-mCitrine* mouse showing expression in endothelium (left), vascular labeled with FITC-dextran (center), and a merged image (right).

(C) A penetrating arteriole (green, top) and endfoot labeled with Rhod2-AM (red, bottom), showing aCSF (left), the presence of compound 21 (center), and the difference (right).

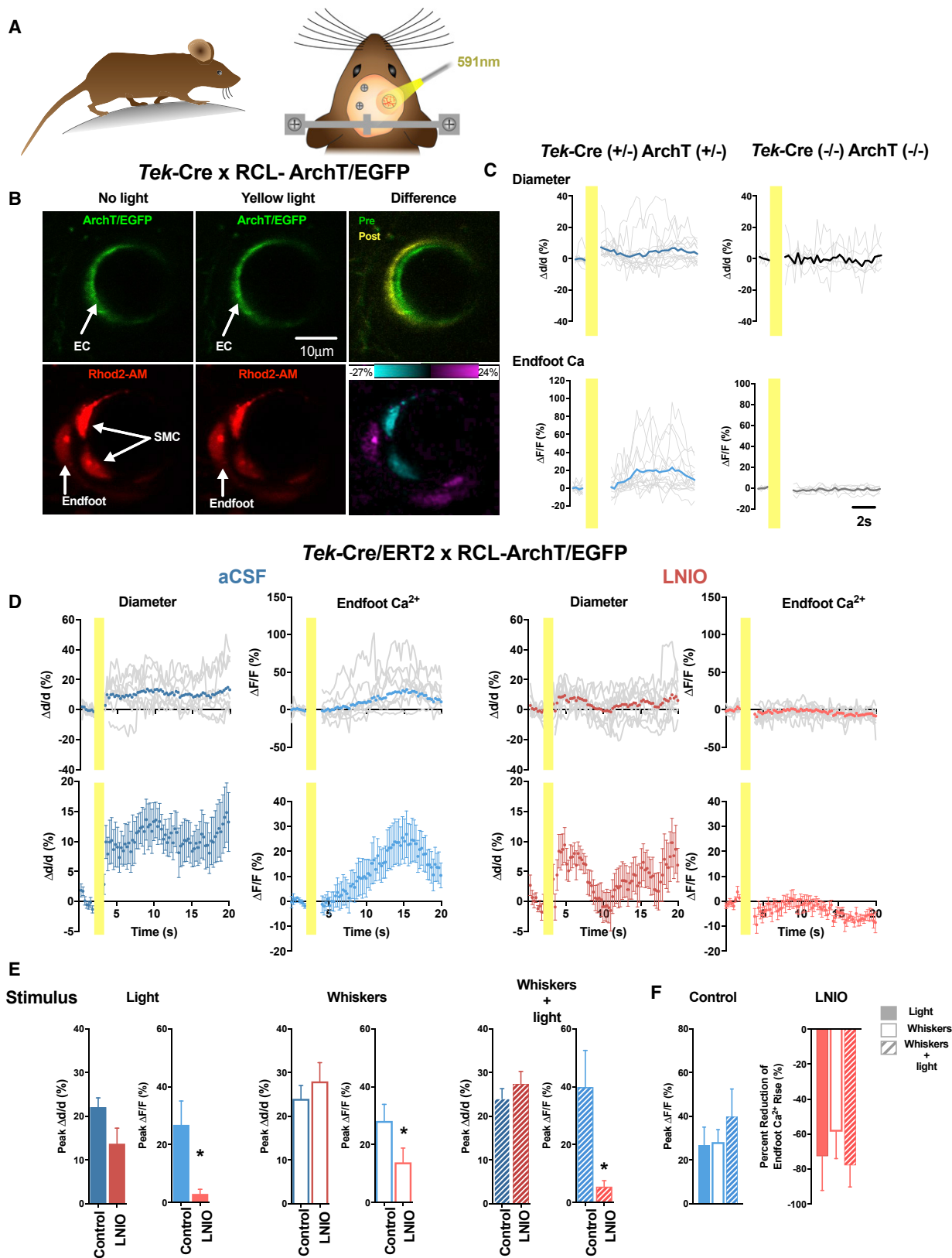
(D) Representative traces of arteriole diameter and endfoot  $Ca^{2+}$  of *Tek-Cre/ERT2-* and *GqDREADD-negative* mice (gray) and positive mice (color) in response to compound 21.

(E) Summary data of arteriole diameter in compound 21 in the presence or absence of LNIO (300  $\mu$ M) (\* $p$  = 0.002; \*\* $p$  = 0.02, paired t test;  $n$  = 10 animals). Data are mean  $\pm$  SEM.

(F) Summary data of average endfoot  $Ca^{2+}$  change with compound 21 in the presence or absence of LNIO (\* $p$  = 0.006 aCSF versus compound 21 and \*\* $p$  = 0.03 compound 21 versus compound 21 + LNIO; paired t test;  $n$  = 10 animals).

that, when light activates ArchT,  $H^+$  ions would be extruded from the endothelium, causing hyperpolarization. This would also hyperpolarize smooth muscle cells via charge transfer across myo-endothelial gap junctions, causing a drop in smooth muscle cell  $Ca^{2+}$  and consequent arteriole dilation (Segal, 2015). Endothelial hyperpolarization initiates vascular electrical conduction (Do-meier and Segal, 2007), which is a component of functional hyper-

emia (Longden et al., 2017). We loaded Rhod-2 AM in astrocytes and delivered 591-nm laser light onto the center of the window using an optical fiber ( $\sim$ 1.5-mm diameter spot size). By shining the light for 1 s and titrating the laser power on successive trials, we could eventually evoke arteriole dilation ( $\Delta d/d$  = 7.2%  $\pm$  2.4%,  $p$  < 0.001) (laser power = 10–15 mW out of the fiber), which was followed by an increase in endfoot  $Ca^{2+}$  ( $\Delta F/F$  = 21.0%  $\pm$  7.0%,



(legend on next page)

n = 15 trials, 5 mice,  $p < 0.001$ ; **Figure 8C**, left). The same experiment performed on *Tek-Cre*- and ArchT/EGFP-negative animals caused neither arteriole dilation ( $2.0\% \pm 3.0\%$ ,  $p = 0.3$ ) nor raised endfoot  $\text{Ca}^{2+}$  ( $-2.6\% \pm 1.1\%$ ,  $p = 0.8$ ; n = 6 trials, 3 mice; **Figure 8C**, right).

Increased blood flow causes increased shear stress along the vessel wall and augments NO production, leading to vasodilation, termed flow-induced vasodilation (Kuo et al., 1990; Rubanyi et al., 1986). Furthermore, vascular electrical conduction and subsequent dilation are followed by a slower, endothelium-derived wave of NO release (Budell et al., 2003; Tallini et al., 2007). Therefore, we examined the role of NO in facilitating the endfoot  $\text{Ca}^{2+}$  signal in response to opto-mediated arteriole dilation. These experiments used conditional *Tek-Cre/ERT2* x ArchT/EGFP mice. We first ensured a control response from arterioles and endfeet to yellow light in superfused aCSF and then examined the effect of LNIO in a paired fashion. In the presence of LNIO, we found that light-evoked arteriole dilation and endfoot  $\text{Ca}^{2+}$  elevation were significantly attenuated (control  $\Delta d/d = 22.1\% \pm 2.1\%$  versus LNIO  $\Delta d/d = 13.8\% \pm 3.6\%$ ,  $p = 0.06$ ; control  $\Delta F/F = 26.8\% \pm 8.2\%$  versus LNIO  $\Delta F/F = 3.0\% \pm 1.6\%$ , n = 14 trials, 5 mice,  $p = 0.006$ ; **Figures 8D** and **8E**, left), implicating endothelium-derived NO in the effect.

Given that endfoot  $\text{Ca}^{2+}$  increased to both whisker-evoked dilation and light-induced vasodilation in an NO-dependent manner, we tested the hypothesis that each route converged onto a common eNOS pathway. For this, we measured dilation and endfoot  $\text{Ca}^{2+}$  to each stimulation given alone and when combined. In *Tek-Cre/ERT2* x ArchT/EGFP animals, whisker stimulation generated arteriole dilation (control  $\Delta d/d = 24.0\% \pm 3.1\%$ ), followed by a delayed endfoot  $\text{Ca}^{2+}$  signal ( $\Delta F/F = 28.2\% \pm 5.7\%$ , n = 14 trials, 5 mice; **Figure 8E**, center), and only the  $\text{Ca}^{2+}$  change was sensitive to LNIO treatment ( $\Delta d/d = 28\% \pm 4.3\%$ ,  $p = 0.5$ ;  $\Delta F/F = 13.87\% \pm 4.9\%$ , n = 14 trials, 5 mice,  $p = 0.005$ ; **Figure 8E**, center). We then tested whether we could occlude any further increase in sensation-evoked endfoot  $\text{Ca}^{2+}$  when whisker stimulation was given in the presence of light. Indeed, we found that whisker stimulation plus yellow light did not enhance endfoot  $\text{Ca}^{2+}$  to a greater degree compared with either manipulation alone (light,  $26.83\% \pm 8.2\%$ ; whisker stimulation,  $28.2\% \pm 5.7\%$ ; whisker stimulation plus light,  $39.9\% \pm 12.7\%$ ; n = 14 trials; 5 mice;  $p = 0.3$ ; **Figures 8E** and **8F**). Furthermore, LNIO still decreased the evoked endfoot  $\text{Ca}^{2+}$  signal in response to whisker stimulation plus light (control  $\Delta F/F = 39.9\% \pm 12.7\%$  versus

LNIO  $\Delta F/F = 5.5\% \pm 2.1\%$ , n = 14 trials, 5 mice,  $p = 0.03$ ; **Figure 8E**, right), and the degree of this reduction was not different across all three stimulation groups (light:  $-77.6\% \pm 16.1\%$ ; whisker stimulation:  $-43.23\% \pm 17.4\%$ ; whisker stimulation plus light:  $-61.2\% \pm 20.0\%$ , n = 14 trials, 5 mice,  $p = 0.5$ ; **Figure 8F**). These data suggest that arteriole-derived NO can elevate endfoot  $\text{Ca}^{2+}$  and that, during functional hyperemia, this arteriole-to-endfoot pathway is recruited during sensation-driven glutamatergic input to the barrel cortex.

## DISCUSSION

The model we propose is that, during functional hyperemia, glutamate is the primary driver of the delayed astrocyte  $\text{Ca}^{2+}$  elevation. The presence of neuromodulators from increased arousal/locomotion and/or the presence of vascular-derived NO, facilitates the astrocyte  $\text{Ca}^{2+}$  signal. DNQX and APV largely eliminated the astrocyte endfoot  $\text{Ca}^{2+}$  in response to whisker stimulation or in response to a natural running/whisking event despite the fact that the vasodilation was mostly intact. We anticipate that a higher dose of APV would have decreased sensory evoked vasodilation via the NMDA-nNOS pathway by reaching deeper into the cortical mantle as other studies have reported (Busija et al., 2007; Lecrux and Hamel, 2011; Ma et al., 1996). This is because we did observe a reduction in functional hyperemia using the nNOS blocker NPLA. However, NPLA did not reduce endfoot  $\text{Ca}^{2+}$ , suggesting that the effect of APV on astrocyte  $\text{Ca}^{2+}$  was not via neural NMDAR-generated NO. One way these data can be understood is the evidence that brain microvascular endothelium expresses NMDA receptors (Stobart et al., 2013) and, perhaps, that these receptors are responsible for the late endfoot  $\text{Ca}^{2+}$  signal rather than synaptic NMDARs. Garthwaite et al. (1988) showed how NMDAR activation leads to the accumulation of cGMP in the brain, and, based on extracellular NO scavenging experiments, they speculated that the source of NO could be vascular rather than neuronal. How neuronally derived NO fails to affect endfoot  $\text{Ca}^{2+}$  but vasculature-derived NO does may be puzzling. However, the two signaling pathways are likely spatially separated. Electron microscopy (EM) immuno-labeling showed that only 5%–10% of terminals and dendrites in the barrel cortex express nNOS, even around blood vessels (Wang et al., 2005), suggesting that neuronally derived NO affects only targeted points on the vascular network and, thus, would likely not affect all astrocytic endfeet. Conversely, eNOS is ubiquitously expressed by vascular endothelium (Shu et al., 2015). Furthermore, hyperpolarization of deep and small-diameter microvasculature from synaptic

### Figure 8. Arteriole Dilation Triggered by Vascular Optogenetics Evokes Endfoot $\text{Ca}^{2+}$ Activity

- (A) Cartoons depicting the configuration for vascular optogenetics using *Tek-Cre/ERT2* ArchT/EGFP mice and an external 591-nm fiber-coupled laser.  
 (B) A penetrating arteriole with endothelial cells expressing ArchT/EGFP (green top) and an endfoot loaded with Rhod-2 AM (red, bottom). Smooth muscle cells (SMCs) were also loaded with Rhod-2 AM. Shown are images taken prior to (left) and in response to activation of ArchT (center) and difference images (right).  
 (C) Time courses of arteriole diameter and endfoot  $\text{Ca}^{2+}$  of *Tek-Cre* ArchT/EGFP mice in response to 1 s of light (yellow shaded areas). Individual trials are shown in gray. Average traces are shown in color (left). No responses were observed in *Tek-Cre* ArchT/EGFP negative mice (right).  
 (D) Time courses of arteriole diameter and endfoot  $\text{Ca}^{2+}$  of *Tek-Cre/ERT2* ArchT/EGFP mice in response to 1 s of light in aCSF or in the presence of 300  $\mu\text{M}$  LNIO. Top: all trial traces are shown in gray, with average values shown as colored dots. Bottom: averaged data with SEM.  
 (E) Summary data of arteriole diameter and endfoot  $\text{Ca}^{2+}$  in response to 1-s yellow laser light (left,  $*p = 0.006$ ), 5-s whisker stimulation (center,  $*p = 0.005$ ), and laser light + whisker stimulation (right,  $*p = 0.03$ ) in the presence or absence of 300  $\mu\text{M}$  LNIO. Paired t test.  
 (F) Summary data of arteriole diameter (left) and percent reduction of endfoot  $\text{Ca}^{2+}$  elevation (right) to 3 different stimulation regimens. Data are mean  $\pm$  SEM.

activity begins a retrograde conducted response that helps dilate upstream contractile vasculature. This phenomenon travels at  $\sim 2$  mm/s and accounts, at least partially, for fast functional hyperemia (Chen et al., 2014; Longden et al., 2017). Notably, work from other vascular beds showed that a slower, secondary wave follows the ascending hyperpolarization, involving endothelial  $\text{Ca}^{2+}$  elevation and the release of NO, which occurs on the order of  $\sim 100$   $\mu\text{m/s}$  (Tallini et al., 2007). Thus, one would expect a large, delayed wave of vascular NO that follows initial fast vasodilation. This is consistent with our data that describe a delayed endfoot  $\text{Ca}^{2+}$  that follows vasodilation and is enhanced by NO.

One pitfall to our work is acute inflammatory effects of the cranial window. Although mice were on dexamethasone to minimize acute inflammation and brain swelling from surgery, this is an important caveat, and it is necessary to compare our findings with a thinned-skull preparation. Furthermore, our data do not examine deeper layers of the cortex. Previous work suggests that functional hyperemia is initiated in the deepest cortical layer (VI) (Uhlirva et al., 2016) and propagates up to the pial surface (Chen et al., 2014). Capillaries may respond before penetrating arterioles during functional hyperemia (Biesecker et al., 2016; Hall et al., 2014; Longden et al., 2017), which is somewhat consistent with our data. However, the onset of peri-capillary endfoot  $\text{Ca}^{2+}$  signals was still slower than the initiation of functional hyperemia ( $\sim 3.5$  s versus 0.8 s).

It is well defined that astroglia can sense glutamatergic synaptic transmission (Nimmerjahn et al., 2009; Schummers et al., 2008; Zonta et al., 2003) and signals arising from the noradrenergic and cholinergic systems (Bekar et al., 2008; Ding et al., 2013; Paukert et al., 2014; Takata et al., 2011). *In vivo*, the release of endogenous norepinephrine and acetylcholine (ACh) is associated with arousal, attention, and vigilance (Aoki et al., 1998; Polack et al., 2013; Vaucher and Hamel, 1995). Direct electrical stimulation of the *locus coeruleus* (Bekar et al., 2008; Ding et al., 2013) or *nucleus basalis* (Chen et al., 2012; Takata et al., 2011) or locomotion (Paukert et al., 2014) have all been shown to induce or enhance  $\text{Ca}^{2+}$  transients in cortical astrocytes, which is consistent with our data. In the absence of locomotion, no whisking, and little arousal (continuous quiet), the glutamatergic thalamocortical afferents would form the primary input to the barrel cortex in response to whisker stimulation, which is consistent with the smaller degree of astrocyte activation we observed. Our data are also consistent with a lack of astrocyte signals observed in lightly sedated mice (Bonder and McCarthy, 2014), where arousal/attention is below normal. In fact, our data showed that whisker-stimulation-initiated running (quiet-to-running)—a behavior previously known to trigger activation of Bergmann glia in the cerebellum (Nimmerjahn et al., 2009) and astrocytes in the visual cortex (Paukert et al., 2014)—induced strong astrocyte  $\text{Ca}^{2+}$  elevation in the barrel cortex.

Finally, our data point to an important role of vascular NO in a novel form of arteriole-to-endfoot communication. Kim et al. (2015) demonstrated that astrocytes display an elevation in  $\text{Ca}^{2+}$  to the myogenic response via mechano-sensitive and  $\text{Ca}^{2+}$ -permeable TRPV4 channels in endfeet. However, this is

a vasoconstriction to increased luminal pressure, and we were likely studying a different cell-cell pathway because it is unlikely that (1) the vasodilation we observed was the result of a systemic drop in blood pressure and (2) that the myogenic response would use the same mechanism as functional hyperemia. The pressure-TRPV4 mechanism is also proposed to go beyond affecting just astrocyte  $\text{Ca}^{2+}$  and can ultimately affect neural activity (Kim et al., 2016). It would be interesting to better understand whether the facilitation of astrocyte  $\text{Ca}^{2+}$  by vascularly derived NO can affect neural/synaptic function. Recent data exploiting optogenetic control of vasculature *in vivo* showed that direct control of blood flow did not affect the power of the gamma band in local field potential recordings (Mateo et al., 2017). Although this argues against the vasculo-neuronal hypothesis, other aspects of neural excitability or synaptic properties should be examined in future studies.

Collectively, our data support the idea that astrocyte activation *in vivo* may rely on integrating signals from multiple inputs: glutamatergic synapses, neuromodulatory afferents, and vascular-derived NO. This study provides a new platform to explore the role of astrocyte  $\text{Ca}^{2+}$  transients in the behaving animal.

## STAR★METHODS

Detailed methods are provided in the online version of this paper and include the following:

- KEY RESOURCE TABLE
- CONTACT FOR REAGENT AND RESOURCE SHARING
- EXPERIMENTAL MODEL AND SUBJECT DETAILS
  - Animals
- METHOD DETAILS
  - Awake *In Vivo* Preparation
  - Calcium Indicator loading
  - Vessel Indicators
  - Two-Photon Fluorescence Microscopy
  - Behavior Capture
  - Whisker Stimulation
  - Light Stimulation
  - Pharmacology
- QUANTIFICATION AND STATISTICAL ANALYSIS
  - Data Analysis
  - Machine Learning
  - Stats

## SUPPLEMENTAL INFORMATION

Supplemental Information includes five videos and can be found with this article online at <https://doi.org/10.1016/j.neuron.2018.09.045>.

A video abstract is available at <https://doi.org/10.1016/j.neuron.2018.09.045#mmc6>.

## ACKNOWLEDGMENTS

This work was supported by the Canadian Institutes of Health Research. G.R.G. was supported by Canada Research Chairs. C.H.T.T. was supported by Alberta Innovates Health Solutions. G.P. was supported by the Hotchkiss Brain Institute. We thank Dr. Craig Brown at the University of Victoria for supplying us with *Tek-Cre/ERT2* mice. We thank the developers and distributors of ScanImage open-source control and acquisition software for two-photon

laser-scanning microscopy. We thank Annie Hotchkiss for supplying the 3D model cartoon of the awake *in vivo* experimental setup.

#### AUTHOR CONTRIBUTIONS

Conceptualization, C.H.T.T. and G.R.G.; Methodology, C.H.T.T. and G.R.G.; Investigation, C.H.T.T.; Formal analysis, C.H.T.T. and G.P.; Writing - Original Draft, C.H.T.T. and G.R.G.; Writing - Review & Editing, C.H.T.T., G.P. and G.R.G.; Supervision, G.R.G.

#### DECLARATION OF INTERESTS

The authors declare no competing interests

Received: September 16, 2016

Revised: June 25, 2018

Accepted: September 24, 2018

Published: October 25, 2018

#### REFERENCES

- Agarwal, A., Wu, P.-H., Hughes, E.G., Fukaya, M., Tischfield, M.A., Langseth, A.J., Wirtz, D., and Bergles, D.E. (2017). Transient Opening of the Mitochondrial Permeability Transition Pore Induces Microdomain Calcium Transients in Astrocyte Processes. *Neuron* 93, 587–605.e7.
- Aoki, C., Venkatesan, C., Go, C.G., Forman, R., and Kurose, H. (1998). Cellular and subcellular sites for noradrenergic action in the monkey dorsolateral prefrontal cortex as revealed by the immunocytochemical localization of noradrenergic receptors and axons. *Cereb. Cortex* 8, 269–277.
- Arabzadeh, E., Zorzin, E., and Diamond, M.E. (2005). Neuronal encoding of texture in the whisker sensory pathway. *PLoS Biol.* 3, e17.
- Arganda-Carreras, I., Kaynig, V., Rueden, C., Eliceiri, K.W., Schindelin, J., Cardona, A., and Sebastian Seung, H. (2017). Trainable Weka Segmentation: a machine learning tool for microscopy pixel classification. *Bioinformatics* 33, 2424–2426.
- Bal-Price, A., Moneer, Z., and Brown, G.C. (2002). Nitric oxide induces rapid, calcium-dependent release of vesicular glutamate and ATP from cultured rat astrocytes. *Glia* 40, 312–323.
- Bekar, L.K., He, W., and Nedergaard, M. (2008). Locus coeruleus alpha-adrenergic-mediated activation of cortical astrocytes *in vivo*. *Cereb. Cortex* 18, 2789–2795.
- Bezzi, P., Carmignoto, G., Pasti, L., Vesce, S., Rossi, D., Rizzi, B.L., Pozzan, T., and Volterra, A. (1998). Prostaglandins stimulate calcium-dependent glutamate release in astrocytes. *Nature* 391, 281–285.
- Biesecker, K.R., Srienc, A.I., Shimoda, A.M., Agarwal, A., Bergles, D.E., Kofuji, P., and Newman, E.A. (2016). Glial Cell Calcium Signaling Mediates Capillary Regulation of Blood Flow in the Retina. *J. Neurosci.* 36, 9435–9445.
- Bindocci, E., Savtchouk, I., Liaudet, N., Becker, D., Carriero, G., and Volterra, A. (2017). Three-dimensional Ca<sup>2+</sup> imaging advances understanding of astrocyte biology. *Science* 356, eaai8185.
- Bonder, D.E., and McCarthy, K.D. (2014). Astrocytic Gq-GPCR-linked IP3R-dependent Ca<sup>2+</sup> signaling does not mediate neurovascular coupling in mouse visual cortex *in vivo*. *J. Neurosci.* 34, 13139–13150.
- Budel, S., Bartlett, I.S., and Segal, S.S. (2003). Homocellular conduction along endothelium and smooth muscle of arterioles in hamster cheek pouch: unmasking an NO wave. *Circ. Res.* 93, 61–68.
- Busija, D., Bari, F., Domoki, F., and Louis, T. (2007). Mechanisms involved in the cerebrovascular dilator effects of N-methyl-D-aspartate in cerebral cortex. *Brain Research Reviews* 56, 89–100.
- Cai, C., Fordsmann, J.C., Jensen, S.H., Gesslein, B., Lonstrup, M., Hald, B.O., Zambach, S.A., Brodin, B., and Lauritzen, M.J. (2018). Stimulation-induced increases in cerebral blood flow and local capillary vasoconstriction depend on conducted vascular responses. *Proc. Natl. Acad. Sci. USA* 115, E5796–E5804.
- Chatterjee, S., Fujiwara, K., Pérez, N.G., Ushio-Fukai, M., and Fisher, A.B. (2015). Mechanosignaling in the vasculature: emerging concepts in sensing, transduction and physiological responses. *Am. J. Physiol. Heart Circ. Physiol.* 308, H1451–H1462.
- Chen, N., Sugihara, H., Sharma, J., Perea, G., Petravicz, J., Le, C., and Sur, M. (2012). Nucleus basalis-enabled stimulus-specific plasticity in the visual cortex is mediated by astrocytes. *Proc. Natl. Acad. Sci. USA* 109, E2832–E2841.
- Chen, B.R., Kozberg, M.G., Bouchard, M.B., Shaik, M.A., and Hillman, E.M.C. (2014). A critical role for the vascular endothelium in functional neurovascular coupling in the brain. *J. Am. Heart Assoc.* 3, e000787.
- Dani, J.W., and Smith, S.J. (1995). The triggering of astrocytic calcium waves by NMDA-induced neuronal activation. *Ciba Found. Symp.* 188, 195–205, discussion 205–209.
- Deschênes, M., Moore, J., and Kleinfeld, D. (2012). Sniffing and whisking in rodents. *Curr. Opin. Neurobiol.* 22, 243–250.
- Ding, F., O'Donnell, J., Thrane, A.S., Zeppenfeld, D., Kang, H., Xie, L., Wang, F., and Nedergaard, M. (2013).  $\alpha$ 1-Adrenergic receptors mediate coordinated Ca<sup>2+</sup> signaling of cortical astrocytes in awake, behaving mice. *Cell Calcium* 54, 387–394.
- Dombeck, D.A., Khabbaz, A.N., Collman, F., Adelman, T.L., and Tank, D.W. (2007). Imaging large-scale neural activity with cellular resolution in awake, mobile mice. *Neuron* 56, 43–57.
- Domeier, T.L., and Segal, S.S. (2007). Electromechanical and pharmacomechanical signalling pathways for conducted vasodilatation along endothelium of hamster feed arteries. *J. Physiol.* 579, 175–186.
- Fergus, A., and Lee, K.S. (1997). Regulation of cerebral microvessels by glutamatergic mechanisms. *Brain Res.* 754, 35–45.
- Fiacco, T.A., and McCarthy, K.D. (2004). Intracellular astrocyte calcium waves *in situ* increase the frequency of spontaneous AMPA receptor currents in CA1 pyramidal neurons. *J. Neurosci.* 24, 722–732.
- Garthwaite, J., Charles, S.L., and Chess-Williams, R. (1988). Endothelium-derived relaxing factor release on activation of NMDA receptors suggests role as intercellular messenger in the brain. *Nature* 336, 385–388.
- Girouard, H., Bonev, A.D., Hannah, R.M., Meredith, A., Aldrich, R.W., and Nelson, M.T. (2010). Astrocytic endfoot Ca<sup>2+</sup> and BK channels determine both arteriolar dilation and constriction. *Proc. Natl. Acad. Sci. USA* 107, 3811–3816.
- Gordon, G.R.J., Choi, H.B., Rungta, R.L., Ellis-Davies, G.C.R., and MacVicar, B.A. (2008). Brain metabolism dictates the polarity of astrocyte control over arterioles. *Nature* 456, 745–749.
- Gordon, G.R.J., Iremonger, K.J., Kantevari, S., Ellis-Davies, G.C.R., MacVicar, B.A., and Bains, J.S. (2009). Astrocyte-mediated distributed plasticity at hypothalamic glutamate synapses. *Neuron* 64, 391–403.
- Hall, C.N., Reynell, C., Gesslein, B., Hamilton, N.B., Mishra, A., Sutherland, B.A., O'Farrell, F.M., Buchan, A.M., Lauritzen, M., and Attwell, D. (2014). Capillary pericytes regulate cerebral blood flow in health and disease. *Nature* 508, 55–60.
- Jiang, M.H., Kaku, T., Hada, J., and Hayashi, Y. (2002). Different effects of eNOS and nNOS inhibition on transient forebrain ischemia. *Brain Res.* 946, 139–147.
- Kang, J., Jiang, L., Goldman, S.A., and Nedergaard, M. (1998). Astrocyte-mediated potentiation of inhibitory synaptic transmission. *Nat. Neurosci.* 1, 683–692.
- Kim, K.J., Iddings, J.A., Stern, J.E., Blanco, V.M., Croom, D., Kirov, S.A., and Filosa, J.A. (2015). Astrocyte contributions to flow/pressure-evoked parenchymal arteriole vasoconstriction. *J. Neurosci.* 35, 8245–8257.
- Kim, K.J., Ramiro Diaz, J., Iddings, J.A., and Filosa, J.A. (2016). Vasculo-Neuronal Coupling: Retrograde Vascular Communication to Brain Neurons. *J. Neurosci.* 36, 12624–12639.
- Kozlov, A.S., Angulo, M.C., Audinat, E., and Charpak, S. (2006). Target cell-specific modulation of neuronal activity by astrocytes. *Proc. Natl. Acad. Sci. USA* 103, 10058–10063.

- Krupa, D.J., Wiest, M.C., Shuler, M.G., Laubach, M., and Nicolelis, M.A.L. (2004). Layer-specific somatosensory cortical activation during active tactile discrimination. *Science* 304, 1989–1992.
- Kuo, L., Davis, M.J., and Chilian, W.M. (1990). Endothelium-dependent, flow-induced dilation of isolated coronary arterioles. *Am. J. Physiol.* 259, H1063–H1070.
- Lecrux, C., and Hamel, E. (2011). The neurovascular unit in brain function and disease. *Acta. Physiol. (Oxf)*. 203, 47–59.
- Lind, B.L., Brazhe, A.R., Jessen, S.B., Tan, F.C.C., and Lauritzen, M.J. (2013). Rapid stimulus-evoked astrocyte Ca<sup>2+</sup> elevations and hemodynamic responses in mouse somatosensory cortex in vivo. *Proc. Natl. Acad. Sci. USA* 110, E4678–E4687.
- Longden, T.A., Dabertrand, F., Koide, M., Gonzales, A.L., Tykocki, N.R., Brayden, J.E., Hill-Eubanks, D., and Nelson, M.T. (2017). Capillary K<sup>+</sup>-sensing initiates retrograde hyperpolarization to increase local cerebral blood flow. *Nat. Neurosci.* 20, 717–726.
- Ma, J., Meng, W., Ayata, C., Huang, P.L., Fishman, M.C., and Moskowitz, M.A. (1996). L-NNA-sensitive regional cerebral blood flow augmentation during hypercapnia in type III NOS mutant mice. *Am. J. Physiol.* 271, H1717–H1719.
- Ma, Z., Stork, T., Bergles, D.E., and Freeman, M.R. (2016). Neuromodulators signal through astrocytes to alter neural circuit activity and behaviour. *Nature* 539, 428–432.
- Masamoto, K., Fukuda, M., Vazquez, A., and Kim, S.-G. (2009). Dose-dependent effect of isoflurane on neurovascular coupling in rat cerebral cortex. *Eur. J. Neurosci.* 30, 242–250.
- Mateo, C., Knutsen, P.M., Tsai, P.S., Shih, A.Y., and Kleinfeld, D. (2017). Entrainment of Arteriole Vasomotor Fluctuations by Neural Activity Is a Basis of Blood-Oxygenation-Level-Dependent “Resting-State” Connectivity. *Neuron* 96, 936–948.e3.
- Mehina, E.M.F., Murphy-Royal, C., and Gordon, G.R. (2017). Steady-State Free Ca<sup>2+</sup> in Astrocytes Is Decreased by Experience and Impacts Arteriole Tone. *J. Neurosci.* 37, 8150–8165.
- Mulligan, S.J., and MacVicar, B.A. (2004). Calcium transients in astrocyte endfeet cause cerebrovascular constrictions. *Nature* 431, 195–199.
- Muralidhar, S., Wang, Y., and Markram, H. (2013). Synaptic and cellular organization of layer 1 of the developing rat somatosensory cortex. *Front Neuroanat.* 7, 52.
- Nimmerjahn, A., Mukamel, E.A., and Schnitzer, M.J. (2009). Motor behavior activates Bergmann glial networks. *Neuron* 62, 400–412.
- Nizar, K., Uhlirva, H., Tian, P., Saisan, P.A., Cheng, Q., Reznichenko, L., Weldy, K.L., Steed, T.C., Sridhar, V.B., MacDonald, C.L., et al. (2013). In vivo stimulus-induced vasodilation occurs without IP<sub>3</sub> receptor activation and may precede astrocytic calcium increase. *J. Neurosci.* 33, 8411–8422.
- Norup Nielsen, A., and Lauritzen, M. (2001). Coupling and uncoupling of activity-dependent increases of neuronal activity and blood flow in rat somatosensory cortex. *J. Physiol.* 533, 773–785.
- Otsu, Y., Couchman, K., Lyons, D.G., Collot, M., Agarwal, A., Mallet, J.-M., Pfrieger, F.W., Bergles, D.E., and Chrapak, S. (2015). Calcium dynamics in astrocyte processes during neurovascular coupling. *Nat. Neurosci.* 18, 210–218.
- Palmer, R.M., Ferrige, A.G., and Moncada, S. (1987). Nitric oxide release accounts for the biological activity of endothelium-derived relaxing factor. *Nature* 327, 524–526.
- Parpura, V., and Haydon, P.G. (2000). Physiological astrocytic calcium levels stimulate glutamate release to modulate adjacent neurons. *Proc. Natl. Acad. Sci. USA* 97, 8629–8634.
- Pastl, L., Pozzan, T., and Carmignoto, G. (1995). Long-lasting changes of calcium oscillations in astrocytes: A new form of glutamate-mediated plasticity. *J. Biol. Chem.* 270, 15203–15210.
- Paukert, M., Agarwal, A., Cha, J., Doze, V.A., Kang, J.U., and Bergles, D.E. (2014). Norepinephrine controls astroglial responsiveness to local circuit activity. *Neuron* 82, 1263–1270.
- Polack, P.-O., Friedman, J., and Golshani, P. (2013). Cellular mechanisms of brain state-dependent gain modulation in visual cortex. *Nat. Neurosci.* 16, 1331–1339.
- Rosenegger, D.G., Tran, C.H., LeDue, J., Zhou, N., and Gordon, G.R. (2014). A high performance, cost-effective, open-source microscope for scanning two-photon microscopy that is modular and readily adaptable. *PLoS One* 9, e110475.
- Rosenegger, D.G., Tran, C.H.T., Wamsteeker Cusulin, J.I., and Gordon, G.R. (2015). Tonic Local Brain Blood Flow Control by Astrocytes Independent of Phasic Neurovascular Coupling. *J. Neurosci.* 35, 13463–13474.
- Rubanyi, G.M., Romero, J.C., and Vanhoutte, P.M. (1986). Flow-induced release of endothelium-derived relaxing factor. *Am. J. Physiol.* 250, H1145–H1149.
- Schindelin, J., Arganda-Carreras, I., Frise, E., Kaynig, V., Longair, M., Pietzsch, T., Preibisch, S., Rueden, C., Saalfeld, S., Schmid, B., et al. (2012). Fiji: an open-source platform for biological-image analysis. *Nat. Methods* 9, 676–682.
- Schulz, K., Sydekum, E., Krueppel, R., Engelbrecht, C.J., Schlegel, F., Schröter, A., Rudin, M., and Helmchen, F. (2012). Simultaneous BOLD fMRI and fiber-optic calcium recording in rat neocortex. *Nat. Methods* 9, 597–602.
- Schummers, J., Yu, H., and Sur, M. (2008). Tuned responses of astrocytes and their influence on hemodynamic signals in the visual cortex. *Science* 320, 1638–1643.
- Segal, S.S. (2015). Integration and modulation of intercellular signaling underlying blood flow control. *J. Vasc. Res.* 52, 136–157.
- Shih, A.Y., Mateo, C., Drew, P.J., Tsai, P.S., and Kleinfeld, D. (2012). A polished and reinforced thinned-skull window for long-term imaging of the mouse brain. *J. Vis. Exp.* (61), 3742.
- Shu, X., Keller, T.C.S., 4th, Begandt, D., Butcher, J.T., Biver, L., Keller, A.S., Columbus, L., and Isakson, B.E. (2015). Endothelial nitric oxide synthase in the microcirculation. *Cell. Mol. Life Sci.* 72, 4561–4575.
- Sofroniew, N.J., and Svoboda, K. (2015). Whisking. *Curr. Biol.* 25, R137–R140.
- Srinivasan, R., Huang, B.S., Venugopal, S., Johnston, A.D., Chai, H., Zeng, H., Golshani, P., and Khakh, B.S. (2015). Ca<sup>2+</sup> signaling in astrocytes from *Ip3r2(-/-)* mice in brain slices and during startle responses in vivo. *Nat. Neurosci.* 18, 708–717.
- Srinivasan, R., Lu, T.-Y., Chai, H., Xu, J., Huang, B.S., Golshani, P., Coppola, G., and Khakh, B.S. (2016). New Transgenic Mouse Lines for Selectively Targeting Astrocytes and Studying Calcium Signals in Astrocyte Processes In Situ and In Vivo. *Neuron* 92, 1181–1195.
- Stobart, J.L.L., Lu, L., Anderson, H.D.I., Mori, H., and Anderson, C.M. (2013). Astrocyte-induced cortical vasodilation is mediated by D-serine and endothelial nitric oxide synthase. *Proc. Natl. Acad. Sci. USA* 110, 3149–3154.
- Stobart, J.L., Ferrari, K.D., Barrett, M.J.P., Glück, C., Stobart, M.J., Zuend, M., and Weber, B. (2018). Cortical Circuit Activity Evokes Rapid Astrocyte Calcium Signals on a Similar Timescale to Neurons. *Neuron* 98, 726–735.e4.
- Straub, S.V., Bonev, A.D., Wilkerson, M.K., and Nelson, M.T. (2006). Dynamic inositol trisphosphate-mediated calcium signals within astrocyte endfeet underlie vasodilation of cerebral arterioles. *J. Gen. Physiol.* 128, 659–669.
- Takano, T., Tian, G.-F., Peng, W., Lou, N., Libionka, W., Han, X., and Nedergaard, M. (2006). Astrocyte-mediated control of cerebral blood flow. *Nat. Neurosci.* 9, 260–267.
- Takano, T., Han, X., Deane, R., Zlokovic, B., and Nedergaard, M. (2007). Two-photon imaging of astrocytic Ca<sup>2+</sup> signaling and the microvasculature in experimental mice models of Alzheimer’s disease. *Ann. N Y Acad. Sci.* 1097, 40–50.
- Takata, N., Mishima, T., Hisatsune, C., Nagai, T., Ebisui, E., Mikoshiba, K., and Hirase, H. (2011). Astrocyte calcium signaling transforms cholinergic modulation to cortical plasticity in vivo. *J. Neurosci.* 31, 18155–18165.
- Tallini, Y.N., Brekke, J.F., Shui, B., Doran, R., Hwang, S.-M., Nakai, J., Salama, G., Segal, S.S., and Kotlikoff, M.I. (2007). Propagated endothelial Ca<sup>2+</sup> waves and arteriolar dilation in vivo: measurements in Cx40BAC GCaMP2 transgenic mice. *Circ. Res.* 101, 1300–1309.

- Thrane, A.S., Rangroo Thrane, V., Zeppenfeld, D., Lou, N., Xu, Q., Nagelhus, E.A., and Nedergaard, M. (2012). General anesthesia selectively disrupts astrocyte calcium signaling in the awake mouse cortex. *Proc. Natl. Acad. Sci. USA* *109*, 18974–18979.
- Tian, P., Teng, I.C., May, L.D., Kurz, R., Lu, K., Scadeng, M., Hillman, E.M.C., De Crespigny, A.J., D'Arceuil, H.E., Mandeville, J.B., et al. (2010). Cortical depth-specific microvascular dilation underlies laminar differences in blood oxygenation level-dependent functional MRI signal. *Proc. Natl. Acad. Sci. USA* *107*, 15246–15251.
- Tran, C.H.T., and Gordon, G.R. (2015a). Astrocyte and microvascular imaging in awake animals using two-photon microscopy. *Microcirculation* *22*, 219–227.
- Tran, C.H.T., and Gordon, G.R. (2015b). Acute two-photon imaging of the neurovascular unit in the cortex of active mice. *Front. Cell. Neurosci.* *9*, 11.
- Uhlirova, H., Kılıç, K., Tian, P., Thunemann, M., Desjardins, M., Saisan, P.A., Sakadžić, S., Ness, T.V., Mateo, C., Cheng, Q., et al. (2016). Cell type specificity of neurovascular coupling in cerebral cortex. *eLife* *5*, e14315.
- Vaucher, E., and Hamel, E. (1995). Cholinergic basal forebrain neurons project to cortical microvessels in the rat: electron microscopic study with anterogradely transported Phaseolus vulgaris leucoagglutinin and choline acetyltransferase immunocytochemistry. *J. Neurosci.* *15*, 7427–7441.
- Wang, H., Hitron, I.M., Iadecola, C., and Pickel, V.M. (2005). Synaptic and vascular associations of neurons containing cyclooxygenase-2 and nitric oxide synthase in rat somatosensory cortex. *Cereb. Cortex* *15*, 1250–1260.
- Winship, I.R., Plaa, N., and Murphy, T.H. (2007). Rapid astrocyte calcium signals correlate with neuronal activity and onset of the hemodynamic response in vivo. *J. Neurosci.* *27*, 6268–6272.
- Yamada, M., Lamping, K.G., Duttaroy, A., Zhang, W., Cui, Y., Byrmaster, F.P., McKinzie, D.L., Felder, C.C., Deng, C.X., Faraci, F.M., and Wess, J. (2001). Cholinergic dilation of cerebral blood vessels is abolished in M5 muscarinic acetylcholine receptor knockout mice. *Proc. Natl. Acad. Sci. USA* *98*, 14096–14101.
- Zhang, H.Q., Fast, W., Marletta, M.A., Martasek, P., and Silverman, R.B. (1997). Potent and selective inhibition of neuronal nitric oxide synthase by N omega-propyl-L-arginine. *J. Med. Chem.* *40*, 3869–3870.
- Zonta, M., Angulo, M.C., Gobbo, S., Rosengarten, B., Hossmann, K.-A., Pozzan, T., and Carmignoto, G. (2003). Neuron-to-astrocyte signaling is central to the dynamic control of brain microcirculation. *Nat. Neurosci.* *6*, 43–50.

## STAR★METHODS

### KEY RESOURCE TABLE

REAGENT or RESOURCE	SOURCE	IDENTIFIER
Experimental Models: Organisms/Strains		
C57BL/6	Charles River	<a href="https://www.criver.com/products-services/find-model/c57bl6-mouse?region=24">https://www.criver.com/products-services/find-model/c57bl6-mouse?region=24</a>
<i>Slc1a3</i> -Cre/ERT	Jackson Laboratory	Cat# 012586; RRID:IMSR_JAX:012586
RCL-GCaMP3 (Ai38)	Jackson Laboratory	Cat# 014538; RRID:IMSR_JAX:014538
<i>Aldh1l1</i> -Cre/ERT2	Jackson Laboratory	Cat# 029655; RRID:IMSR_JAX:029655
RCL-GCaMP6s (Ai96)	Jackson Laboratory	Cat# 024106; RRID:IMSR_JAX:024106
<i>Tek</i> -Cre	Jackson Laboratory	Cat# 008863; RRID:IMSR_JAX:008863
RCL-ArchT/EGFP (Ai40D)	Jackson Laboratory	Cat# 021188; RRID:IMSR_JAX:021188
<i>Tek</i> -Cre/ERT2	EMMA (via Dr. Craig Brown U Victoria, Canada)	Cat# 00715; RRID:IMSR_EM:00715
CAG-LSL-Gq-DREADD	Jackson Laboratory	Cat# 026220; RRID:IMSR_JAX:026220
Chemicals, Peptides and Recombinant Proteins		
Tamoxifen	Sigma Aldrich	Cat# T5648-1G
DNQX disodium salt	Tocris BioScience	Cat# 2312
D,L-AP5 sodium salt	Tocris BioScience	Cat# 3693
SC58125	Tocris BioScience	Cat# 2895
LNPLA	Tocris BioScience	Cat# 1200
L-NIO dihydrochloride	Tocris BioScience	Cat# 0546
Compound 21 dihydrochloride	HelloBio	Cat# HB6124
Rhod-2/AM	Biotium	Cat# 50024
FITC-dextran 2000KDa	Sigma Aldrich	Ca# FD2000S-5G
Rhod-B-dextran 70KDa	Sigma Aldrich	Cat # R9379-1G
Software and Algorithms		
ScanImage	Vidrio Technologies	<a href="https://vidriotechnologies.com/">https://vidriotechnologies.com/</a>
GraphPad Prism	GraphPad Software Inc.	<a href="https://www.graphpad.com/scientific-software/prism/RRID:SCR_002798">https://www.graphpad.com/scientific-software/prism/RRID:SCR_002798</a>
ImageJ	NIH	<a href="https://imagej.nih.gov/ij/RRID:SCR_003070">https://imagej.nih.gov/ij/RRID:SCR_003070</a>
FIJI	NIH	<a href="http://fiji.sc">http://fiji.sc</a> RRID:SCR_002285
Other		
Custom perforated cover glass	Laser MicroMaching Ltd	<a href="http://www.lasermicromaching.com">http://www.lasermicromaching.com</a> Design available upon request
Custom titanium head-bar	Gordon Lab	Design available upon request
Custom air supported treadmill	See PMID 25698926	n/a
591nm DPSS fiber coupled laser	IkeCool	<a href="http://www.ikecool.com/">www.ikecool.com/</a>
Picospritzer III	Parker	<a href="http://ph.parker.com/us/12051/en/picospritzer-iii-intracellular-microinjection-dispense-systems-picospritzer-micro-dispense-system">http://ph.parker.com/us/12051/en/picospritzer-iii-intracellular-microinjection-dispense-systems-picospritzer-micro-dispense-system</a>

### CONTACT FOR REAGENT AND RESOURCE SHARING

Further information and requests for resources and reagents should be directed to and will be fulfilled by the Lead Contact Grant Gordon ([gordong@ucalgary.ca](mailto:gordong@ucalgary.ca)).

## EXPERIMENTAL MODEL AND SUBJECT DETAILS

### Animals

All animal procedures have been approved by the Animal Care and Use Committee of the University of Calgary. All studies were either performed on male C57BL/6 mice, male *Slc1a3-Cre/ERT* x RCL-GCaMP3 mice (Jax #012586 and #014538, Ai38), male *Aldh111-Cre/ERT2* x RCL-GCaMP6s mice (Jax #029655 and #024106, Ai96), male *Tek-Cre* x RCL-ArchT/EGFP (Jax #008863 and #021188, Ai40D), male *Tek-Cre/ERT2* (EMMA 00715, via Dr. Brown C U Victoria) x RCL-ArchT/EGFP mice, or male or female *Tek-Cre/ERT2* x CAG-LSL-Gq-DREADD (Jax # 026220) mice between P30 to P60. The original background strain from the commercial vendor was used for crosses and all crosses involved heterozygote mice. Positive offspring used for experiments were heterozygotes for each gene/knock-in of interest. For the use of conditional lines (ERT or ERT2), we initiated our acute awake imaging protocol at least two weeks after the last of three consecutive tamoxifen injections (100 mg/kg, 10 mg/mL corn oil stock, Sigma, St. Louise MO USA). Injections started at p19 or up to p35. Animals were kept on a normal 12 hour light and 12 hour dark cycle and had access to food and water *ad libitum*. Animals were group housed until the installation of the head-bar (see below). The experimenter was not blinded to the treatment.

## METHOD DETAILS

### Awake *In Vivo* Preparation

All surgeries used standard aseptic procedures, isoflurane anesthesia, with post-operative pain and infection control as previously described (Tran and Gordon, 2015b). One week before the imaging session, a custom head bar was surgically installed without performing a craniectomy and the animal was then returned to a new home cage to recover for two days (single housing from this point onward). The mouse then began training on a passive air-supported styrofoam ball treadmill under head-restraint (two 30 min sessions on consecutive days) and was habituated to contralateral vibrissae air puff once every minute for 5 s using a picospritzer III (General Valve Corp., Fairfield, USA) under near-infrared illumination. The animal was then allowed to rest for two days in their home cage. On the imaging day, a ~3x3mm cover glass (thickness #0) was installed over the primary somatosensory cortex with bone and dura removed.

### Calcium Indicator loading

In C57BL/6 mice, Rhod-2 AM (15 $\mu$ M, Biotium, Hayward CA USA) ACSF solution containing 0.2% DMSO and 0.006% Pluronic acid was applied to the brain surface for 45 minutes. The solution was replenished to maintain submersion of the brain, and then washed with ACSF for 10 minutes before sealing the window with coverglass.

### Vessel Indicators

Fluorescein isothiocyanate (FITC)-dextran (MW 2,000,000, Sigma) or rhodamine B isothiocyanate (RhodB)-dextran (MW 70,000, Sigma) was tail vein injected (100-200 $\mu$ L of 2.3% (w/v) solution in saline) to visualize the blood plasma. Before imaging the animal recovered on the treadmill with its head immobilized for 30 minutes.

### Two-Photon Fluorescence Microscopy

Fluorescence images were obtained using a custom built *in vivo* two-photon microscope (Rosenegger et al., 2014) fed by a tunable Ti:sapphire laser (Coherent Chameleon, Ultra II, ~4 W avg power, 670-1080 nm, ~80 MHz, 140 fs pulse width), equipped with GaAsP PMTs (Hamamatsu, Japan) and controlled by open-source ScanImage software (<https://wiki.janelia.org/>). We used a Nikon 16X, 0.8NA, 3mm WD objective lens or a Zeiss 40X, 1.0NA, 2.5mm WD objective lens. Rhod-2 was excited at 850 nm and GCaMP3 at 920 nm. Green fluorescence signals were filtered using a 525/50nm BP, and orange/red light was filtered using a 605/70nm BP (Chroma Technology, Bellows Falls VT USA). Bidirectional xy raster scanning was used at a frame rate of 0.98 to 7.81Hz.

### Behavior Capture

A near infrared LED (780 nm) and camera were used to capture simple behaviors such as resting, running and whisking concurrently with two-photon fluorescence imaging for all experimental trials at a frame rate of 14 Hz.

### Whisker Stimulation

For whisker stimulation, a 5 s air puff to the contralateral whiskers was applied using as little air pressure as possible that visibly deflected the whiskers (same as training). The air output was divided to two mounted glass capillary tubes that aim at separate groups of vibrissae in an attempt to stimulate as many whiskers as possible without impacting the face. Penetrating arterioles were identified via their upstream parent pial arterioles, their undulations in diameter, and the appearance of a thick vessel wall.

### Light Stimulation

For optogenetic experiments, 591nm light was used to activate ArchT using a fiber optic coupled DPSS laser (IkeCool, 2355 Westwood Blvd, Los Angeles, US). The fiber (200  $\mu\text{m}$  diameter, 0.22 NA end) was positioned using a manual micromanipulator (Luigs and Neumann, Germany) with a  $\sim 1.5\text{mm}$  laser spot on the center of the window. A 1 s light pulse of 10-15mW avg power was used.

### Pharmacology

For topical superfusion, a custom coverglass with pre-drilled through-holes (7 holes, 175  $\mu\text{m}$  diameter) (Laser Micromachining Ltd) was installed. ACSF was superfused at  $\sim 2\text{ml}/\text{min}$  using a pressurized carbogen delivery system (95%  $\text{O}_2$ , 5%  $\text{CO}_2$ ). ACSF contained (in mM): NaCl, 126; KCl, 2.5;  $\text{NaHCO}_3$ , 25;  $\text{CaCl}_2$ , 1.3;  $\text{MgCl}_2$ , 1.2;  $\text{NaH}_2\text{PO}_4$ , 1.25; glucose, 10; pH 7.4. After stable control data was achieved, pharmacological agents were superfused for 30 minutes prior to testing. All antagonists and agonists were purchased from Tocris BioScience and high concentration stock solutions were made in water following solubility recommendations (except for SC58125 which was dissolved in DMSO; final DMSO concentrations did not exceed 0.1%). DNQX disodium salt (cat# 2312); D,L-AP5 sodium salt (cat# 3693); SC58125 (cat# 2895); LNPLA (*N*<sup>ω</sup>-Propyl-L-arginine hydrochloride)(cat# 1200); L-NIO dihydrochloride (cat# 0546). The DREADD ligand Compound 21 dihydrochloride was purchased from HelloBio.

## QUANTIFICATION AND STATISTICAL ANALYSIS

### Data Analysis

All data was processed using ImageJ. Movement artifacts in the xy plane were corrected for using the template\_matching plugin. The 3D viewer plugin was used to perform three-dimensional rendering of the microvascular network.  $\text{Ca}^{2+}$  responses were calculated as  $\Delta F/F = (F_t - F_{\text{rest}})/F_{\text{rest}} \times 100$ , where  $F_t$  was the fluorescence at a given time and  $F_{\text{rest}}$  was the averaged 2 s baseline fluorescence prior to stimulation. The average extrapolated onset time was estimated by fitting a tangent line to the rising slope of the averaged data and calculating the x-intercept. Trial-based changes were defined as gray value or area that rose above 3 x SD of baseline fluctuations, lasting for at least 0.5 s in individual trials. For trial-based onset times, we used the time point at which the signal from a single trial rose 3 x SD above baseline fluctuation after stim onset. Arteriole diameter ( $\Delta d/d$ ) was calculated using the same general formula above for  $\Delta F/F$ , and was quantified by obtaining a lumen area for every image by thresholding and using particle analysis in ImageJ. Animal behavior video data was analyzed offline and manually assigned a particular activity using techniques previously described (Tran and Gordon, 2015b) and converted into a binary or trinary scale.

### Machine Learning

To calculate RBC flux, we used the Trainable Weka Segmentation tool plugin available in Fiji (Arganda-Carreras et al., 2017; Schindelin et al., 2012) to classify connected image pixels as either 'red blood cell' (RBC) or 'background' on the basis of shape, texture and intensity. Briefly, we: 1) trained a Fast Random Forest classifier on a representative training set consisting of  $\leq 2\%$  of total frames in each stack using default training features and parameters; 2) applied the classifiers to the selected ROIs in the source stacks; 3) used a custom Fiji macro to analyze and write to file the number of individual particles in the 'RBC' class. Segmentation output was also manually assessed for consistency and accuracy of classification, and the training set was expanded to include  $\leq 5\%$  of total frames, as necessary.

### Stats

Statistical analysis used a paired or unpaired t test, or one-way ANOVA as appropriate. Statistical *n* constituted a single experimental trial (such as whiskers stimulation or light stimulation) or a single superfusion experiment (such as compound 21 application) while imaging an astrocyte and arteriole (or capillary) pair. Either a single astrocyte and arteriole pair was examined in a single mouse or two separated astrocyte and arteriole pairs were examined in a single mouse. In each experimental group, at least 3 mice were used. The *n* for each experiment (trials and mice) is reported in the results section. Data are expressed as means  $\pm$  SEM. Significance thresholds were: \**p* < 0.05, \*\**p* < 0.01, \*\*\**p* < 0.001